University of Alberta

Escape of Charged Particles Moving around Weakly Magnetized Black Holes

by

Abdallah M. Al Zahrani

A thesis submitted to the Faculty of Graduate Studies and Research in partial fulfillment of the requirements for the degree of

Doctor of Philosophy

Department of Physics

Spring 2014
Edmonton, Alberta

To my parents

Abstract

Magnetic fields have become an essential ingredient of black hole astrophysics. The study of simplified models of magnetized black holes can shed light on some of the complicated phenomena observed near astrophysical black holes. In this thesis we studied the three-dimensional motion of charged particles in the background of Schwarzschild and Kerr black holes immersed in a weak uniform axisymmetric magnetic field. We studied in particular the escape of charged particles after they are kicked out of circular orbits.

We started with neutral particles and gave analytical conditions for their escape. Unlike with the Schwarzschild black hole, the escape conditions were non-trivial when the black hole is rotating where escape depends essentially on the particle initial position.

It was not possible to give analytical conditions for charged particles escape. The magnetic field renders their equations of motion non-integrable in general. Numerical study of the problem revealed that the dynamics of charged particles near magnetized black holes is generally chaotic. With the help of the basin of attraction approach, we could give empirical formulae for guaranteed escape. We found that the final fate of a charge particle is nearly determined by its proximity to the black holes. No general relationship between the chaoticness in the dynamics and black hole rotation could be found.

Acknowledgement

Before all, praise be to Allah, the cherisher and sustainer of the worlds.

I then would like to thank my supervisor Professor Valeri P. Frolov for his efforts during my program, supporting my participation in "Black Hole VII" conference and inviting me to take a part in "Black Holes: New Horizons" conference, and teaching me "Quantum Mechanics in Curved Spacetime" and "Black Hole Physics." I would as well like to thank Professor Don N. Page for joining my supervisory annual committee, teaching me "Advanced General Relativity" and letting me audit his "Quantum Field Theory I" lectures. Gratitude goes to Professor Sharon Morsink for her efforts as graduate studies chair and a supervisory committee member. I would also like to thank Professor Richard Marchand and Professor David W. Hobill for joining my PhD final exam committee, and Professor Marc de Montigny for joining my PhD candidacy examining committee.

I want to thank the staff of the University of Alberta, in particular the staff of the Libraries, Faculty of Graduate Studies and Research, International Center, Students Success Center and Physics Department. In particular, I like to express my thanks to those in Physics Department: Sarah Derr, Sandra Hamilton and Dr. Isaac Isaac. Special thank is due to Dr. Wladyslaw Rudzinski.

My deepest gratitude is due to my parents, siblings and nieces, and everyone else who offered any kind of help to me.

Finally, I am thankful to the Saudi Arabian Ministry of Higher Education for the sponsorship during my PhD program.

Contents

1 Introduction **1**

1.1 Magnetic Fields near Black Holes 1
1.2 Magnetized Black Holes 2
1.2.1 Exact Solutions 2
1.2.2 Weakly Magnetized Black Holes 4
1.3 Charged Particles Motion near Magnetized Black Holes . . 5
1.4 This Work 6
1.5 Appendix 8

2 Escape of Charged Particles Moving around a Weakly Magnetized Schwarzschild Black Hole **15**

2.1 Introduction 15
2.2 Escape Velocity of a Neutral Particle 16
2.3 Weakly Magnetized Black Holes 19
2.4 Charged Particles near a Magnetized Black Hole 21
2.5 Dimensionless Form of the Equations 22
2.6 Types of the Trajectories 24
2.7 Basin of Attraction Analysis 30
2.7.1 Basin of Attraction Plots 30
2.7.2 Critical Escape Energy and Velocity 31
2.7.3 Near-Critical Behavior 35
2.7.4 Fractal Dimension of the Near-Critical Domains . . 36
2.7.5 Additional Details of the Basins of Attraction Structure. 38
2.8 Summary 38

3 Escape of Charged Particles Moving around a Weakly Magnetized Kerr Black Hole **40**
3.1 Introduction 40
3.2 Escape Velocity of a Neutral Particle 41
3.2.1 Circular Orbits 41
3.2.2 Conditions for Escape from a Circular Orbit 44
3.3 Escape Velocity of a Charged Particle 49
3.3.1 Circular Orbits 49
3.3.2 Three-Dimensional Motion and Conditions for Escape from a Circular Orbit 52
3.3.3 Rotation and Chaoticness 56
3.4 Summary 57
3.5 Appendix 59

4 Conclusion **68**

A Geometrized Units **70**

B Einstein-Maxwell Equations **72**

List of Figures

2.1 Examples of "capture" trajectories. In each case a charged particle is kicked up from its original ISCO at $\rho_o = 2$ for $\ell > 0$. The energy $\mathcal{E}$ after the kick is (a) 1.12 (b) 1.2 and (c) 1.3. 25

2.2 Examples of "capture" trajectories. In each case a charged particle is kicked up from its original ISCO at $\rho_o = 2.5$ for $\ell < 0$. The energy $\mathcal{E}$ after the kick is (**a**) 1.35 (**b**) 1.475 and (**c**) 1.525. 26

2.3 Examples of "escape" trajectories. In each case a charged particle is kicked up from its original ISCO at $\rho_o = 2$ for $\ell > 0$. The energy $\mathcal{E}$ after the kick is (a) 1.025 (b) 1.05 and (c) 1.135. 27

2.4 Examples of "escape" trajectories. In each case a charged particle is kicked up from its original ISCO at $\rho_o = 2.5$ for $\ell < 0$. The energy $\mathcal{E}$ after the kick is (a) 1.415 (b) 1.46 and (c) 1.5. 28

2.5 Basins of attraction for a charged particle kicked from the ISCO of the given ρ_o (horizontal axis) to different energies (vertical axis). The red zones correspond to capture, the green zones correspond to escape to $z \to +\infty$, and the yellow zones correspond to escape to $z \to -\infty$. (a) is for $\ell > 0$ and (b) is for $\ell < 0$. The step size for both ρ and $\mathcal{E}$ is 2.5×10^{-3}. 32

2.6 Critical escape energy for (a) $\ell > 0$ and (b) $\ell < 0$. The curves are given by the empirical expression (2.44) for (a) and by (2.45) for (b). 33

2.7 Critical escape velocity for (a) $\ell > 0$ and (b) $\ell < 0$. 34

2.8 Magnified strips from the fractal region in the basins of attraction. (a) A stripe at $\mathcal{E}$ 1.9 for $\ell > 0$. (b) A strip at $\mathcal{E}$ 2.5 for $\ell < 0$. 35
2.9 The box-counting dimension. Plot (a): $\ln N(\epsilon)$ vs. $\ln(1/\epsilon)$ for $\ell > 0$. Plot (b): $\ln N(\epsilon)$ vs. $\ln(1/\epsilon)$ for $\ell < 0$. 37

3.1 The radius of the last stable circular orbit r_{ms} vs. the black hole's rotation parameter a. 44
3.2 $V_+(r)$ for a particle before (dashed line) and after (solid line) getting kicked to energy $\mathcal{E} = 1$. (a) The particle accelerates away from the black hole after getting kicked from a circular orbit at $r_o = 3M$. (b) The particle accelerates toward the black hole after getting kicked from a circular orbit at $r_0 = 3/2M$. In both cases $a = M$. 46
3.3 $|\dot{\theta}_c|$ (solid) and $|\dot{\theta}_{\mathcal{E}=1}|$ (dashed) vs. r_o for $a = 0.95M$. $|\dot{\theta}_c|$ vanishes at r_{cap} and approached infinity as r_o approaches r_{esc}. 48
3.4 The radius of the initial orbit r_o at which $|\dot{\theta}_c| = |\dot{\theta}_{\mathcal{E}=1}|$ (solid) as a function of a. The dashed curve is r_{cap}. 48
3.5 The dependence of r_{esc}, r_{cap} and r_{ms} (dashed) on a. The escape region is to the right of r_{esc}, the capture region is to the left of r_{cap}, while the critical escape region is the one in between. The dotted line is r_{lc}. 49
3.6 The ISCO's radius r_{ms} dependence on a for different values of the magnetic parameter b for (a) anti–Larmor and (b) Larmor motion. 53
3.7 The ISCO's azimuthal angular momentum $\mathcal{L}_{ms}$ dependence on a for different values of the magnetic parameter b for (a) anti–Larmor and (b) Larmor motion. 60
3.8 The ISCO's energy $\mathcal{E}_{ms}$ dependence on a for different values of the magnetic parameter b for (a) anti–Larmor and (b) Larmor motion. 61

3.9 The trajectories of a charged particle initially at $r_o = 4M$ kicked to three different energies (a): $\mathcal{E} = 1.0890$ (b): $\mathcal{E} = 1.0893$ (c): $\mathcal{E} = 1.0900$. The black hole's spin parameter is $a = 0.5M$ and $b = 0.1M^{-1}$. The particle is scattered to a different final state in every case. 62
3.10 The basin of attraction for a neutral particle. r_{esc} and r_{cap} are shown as well. The black hole's rotation parameter is $a = 0.999M$. 63
3.11 The basins of attraction for a charged particle with $b = 0.1M^{-1}$ for selected a values. 64
3.12 The basins of attraction for a charged particle with $b = -0.1M^{-1}$ for selected a values. 65
3.13 D_f of the basin boundaries vs. a for (a) anti-Larmor motion ($b = 0.1M^{-1}$) and (b) Larmor motion ($b = -0.1M^{-1}$). . . . 66

List of Tables

A.1 Various physical quantities in conventional and geometrized units and the conversion factors. 70
A.2 Some interesting electromagnetic quantities in conventional and geometrized units and the conversion factors. 71

Chapter 1

Introduction

1.1 Magnetic Fields near Black Holes

Magnetic fields are an essential component in black hole astrophysics. They can exist near black holes due to various external sources. A black hole can be magnetized by the large-scale magnetic fields. Magnetic fields have been observed in the galactic and intergalactic media [1][1]. They have typical strengths in the range of 0.1–10^2 microgauss. Although large-scale magnetic fields may have cosmological implications, they are insignificant in black hole astrophysics. A black hole can also be magnetized by a companion magnetic star. Black hole-neutron star binaries are likely to exist [2]. A special class of neutron stars known as magnetars may have the strongest known magnetic fields in the universe. The magnetar SGR 1806-20 has the strongest magnetic field ever known ($B \sim 10^{15}$ gauss [3, 4]). The most significant magnetic fields for black holes are generated by their own accretion disks [5, 6]. Several measurements of magnetic fields around stellar mass and supermassive black holes have been conducted. According to [7, 8], magnetic fields near stellar mass and supermassive black holes have strengths of $\sim 10^8$ gauss and $\sim 10^3 - 10^5$ gauss, respectively.

There are several theoretical reasons urging for the inclusion of mag-

[1] In each chapter the numbers in square brackets refer to the references list at the end of the chapter.

netic fields in black holes astrophysics. Many of these theoretical motivations are related to the bipolar jets of the active galactic nuclei which are believed to be supermassive black holes. Magnetic fields seem to be inevitable to explain the ejection of the jets. Large scale magnetic fields are required to explain the collimation of the jets and the synchrotron radiation from the ultrarelativistic particles in them.

Magnetic fields are essential for black hole accretion disk physics [5, 9]. The mechanism in which matter orbiting a black hole loses angular momentum in accretion flow requires a theoretical explanation. It was suggested that winds and magnetic viscosity in the disk can do the job. There has been observational evidence that winds in the disk of stellar mass black hole are powered by the pressure due to magnetic viscosity (see [10] and references therein).

1.2 Magnetized Black Holes

There are two approaches to magnetized black holes: (1) Exact magnetized solutions and (2) Weakly magnetized solutions. The former are exact solutions of the Einstein-Maxwell equations (see Appendix B), they take into account the back-reaction of the magnetic field on the spacetime geometry. The back-reaction is ignored in the weakly magnetized solutions and the magnetic field is sensed by charged particles only.

1.2.1 Exact Solutions

We introduce here a few exact magnetized black hole solutions and demonstrate their mathematical and conceptual difficulties. The spacetime around a Schwarzschild black hole of mass M immersed in a uniform axisymmetric magnetic field B is given by the Ernst solution [11]. It reads

$$ds^2 = \Lambda \left[-g dt^2 + \frac{dr^2}{g} + r^2 d\theta^2 \right] + \frac{r^2}{\Lambda} \sin^2\theta d\phi^2, \tag{1.1}$$

where $g = 1 - 2M/r$ and $\Lambda = (1 + \frac{1}{4} B^2 r^2 \sin^2\theta)^2$. The electromagnetic

potential is given by

$$A = \frac{2}{B}\left(1 - \Lambda^{-1/2}\right) d\phi. \tag{1.2}$$

Unlike the field components, the Ernst metric is quadratic in B. Keeping only linear terms in B leads to the axisymmetric weak field approximation which will be discussed below. When $M = 0$, the Ernst metric reduces to Melvin metric introduced in [12]. The magnetized Reissner-Nordström and Kerr-Newman solutions are by far more involved. The spacetime around a Kerr-Newman black hole of mass M, spin angular momentum a and charge Q placed in a homogeneous axisymmetric magnetic field B was given in [13, 14]. According to [14] the metric reads

$$\begin{aligned} ds^2 &= H(r,\theta)\left[-f dt^2 + R^2\left(\frac{dr^2}{\Delta} + r^2 d\theta^2\right)\right] \\ &+ \frac{\Sigma \sin^2\theta}{H(r,\theta)R^2}[d\phi - \omega(r,\theta)dt]^2, \end{aligned} \tag{1.3}$$

where $R^2 = r^2 + a^2\cos^2\theta$, $\Delta = r^2 + a^2 + Q^2 - 2Mr$, $f = R^2\Delta\Sigma^{-1}$ and $\Sigma = (r^2 + a^2)^2 - a^2\Delta\sin^2\theta$. The functions $H = H(r,\theta)$ and $\omega = \omega(r,\theta)$ as well as the electromagnetic potential are given in the appendix at the end of this chapter (Sec. 1.5) . The interpretation of the parameters in this solution is non-trivial according to [15]. It is interesting that even when $a = 0$ there will be a $dtd\phi$ term in the metric for any $Q \neq 0$. The magnetization of a Reissner-Nordstörm black hole induces spacetime rotation. Surprisingly, the magnetized Reissner-Nordstörm black hole has an ergo-region [14]. This ergo-region extends to infinity along the poles for any B or Q values. Therefore, the magnetized Reissner-Nordsröm black hole is not asymptotic to Melvin magnetic universe. The structure of the ergo-region is more complicated in the case of the magnetized Kerr-Newman black hole. The geometry is asymptotic to Melvin solution only if the charge has the special value $Q = \frac{B}{aM}(1 + \frac{1}{4}a^2M^2B^4)$. The ergo-region can have different shapes joint and disjoint from the horizon.

The thermodynamics of the magnetized Kerr-Newman black hole was studied in [15, 16]. Since B can be an additional thermodynamic variable,

the first law is modified to

$$dM = \frac{\kappa}{8\pi} dA_H + \Omega dJ + \Phi dQ - \mu dB, \tag{1.4}$$

where μ can be thought of as an induced magnetic moment of the black hole [16]. $\Omega = \Omega_H - \Omega_\infty$ is the difference between the black hole's angular velocity at the horizon and infinity, and $\Phi = \Phi_H - \Phi_\infty$ is the difference in electric potential at the horizon and infinity. To first order in Q, μ reads

$$\mu = aQ(1 + a^2 M^2 B^4) + \mathcal{O}(Q^2). \tag{1.5}$$

1.2.2 Weakly Magnetized Black Holes

Magnetic fields around astrophysical black holes are extremely weak to have significant effect on the spacetime geometry. For a solar mass black hole, the magnetic field around it needs to be of order 10^{19} gauss to have an effect comparable to that of the black hole's mass. This is by far greater than magnetic fields around astrophysical black holes or any known magnetic field. Additionally, we have seen that the exact solutions are extremely cumbersome and physically ambiguous. Therefore it is more economical to ignore the back-reaction of the magnetic field on the metric for all astrophysical purposes. This is known as the *weak field approximation*.

The magnetization procedure introduced by Wald is of special interest. It describes a Kerr black hole immersed in a uniform axisymmetric weak magnetic field [17]. The magnetic field of the accretion disk is well approximated by an axsisymmetric field when the accretion disk is very large compared to the black hole. According to [17], any linear combination of the Killing vectors that a Ricci flat spacetime admits serves as a solution to the Maxwell equations in that spacetime. The rotation of the black hole induces electric fields near the horizon. Due to the electric potential difference between the horizon and infinity the black hole will accrete charges until its charge reaches $Q = 2Ba$.

The Hawking radiation from a Kerr-Newman black hole immersed in a uniform axisymmetric magnetic field was studied numerically in [18].

It was found that the magnetic field increases the evaporation process greatly.

In astrophysical applications, the direction of the magnetic field and the black hole's spin are not usually aligned. The solution for a Kerr black hole in a tilted uniform magnetic field was found in [19] with the help of the Newman-Penrose formalism. The case when a Kerr black hole is drifting in arbitrary direction with respect to a uniform magnetic field in any orientation was treated in [20].

More astrophysically realistic weakly magnetized black hole solutions were worked using the Newman-Penrose formalism. The magnetic fields of an axisymmetric current loop around a Schwarzschild black hole and its dipole part were given in [21]. A generalization that includes eccentric symmetric current loops was made in [22]. The results in [22] were generalized for a Kerr black hole in [19]. Another generalization for the extreme Reissner-Nordström blackhole was conducted in [23].

1.3 Charged Particles Motion near Magnetized Black Holes

The equatorial motion of charged particles near magnetized black holes—where the equations of motion are usually integrable—has been studied extensively. Charged particles equatorial orbits in the Ernst solution were investigated in [24]. Equatorial orbits near a Schwarzschild black hole endowed with a dipole magnetic field were discussed in [25]. A similar study in the background of a weakly magnetized Kerr black hole was conducted in [26]. Two types of test magnetic field were used, a dipole field and uniform axisymmetric field. The innermost stable circular orbits (ISCO)s of a charged particle around a Kerr black hole in a uniform axisymmetric weak magnetic field were studied in [27].

There have been several studies for charged particles motion outside the equatorial plane of magnetized black holes. In [28], it was shown that charged particles are ejected from a Schwarzschild black hole endowed with a toroidal magnetic test field from within a small range near the

poles.

Many other references concluded that the general motion of charged particles near magnetized black holes can be chaotic. The chaotic motion of charged particles in the Ernst spacetime was studied in [29]. It was also demonstrated that the equations of motion appear to be separable in the equatorial plane only. A study of the motion near a Kerr black hole in the presence of a magnetic field generated by a current loop was conducted in [30]. It was shown in it that motion can have chaotic character depending on the initial conditions. The chaotic nature of the dynamics near a Schwarzschild black hole perturbed by an axisymmetric magnetic field was analyzed in [31] using the Poincaré-Melnikov method. In [32], the off-equatorial motion in Kerr background in the presence of a dipole magnetic field was inspected. Using the Poincaré map, it was shown that the motion is chaotic. The authors also concluded that rapid rotation of the black hole weakens the chaotic behavior in particles trajectories. Another study of the off-equatorial motion of charged particles was performed in [33] where the onset of chaos was investigated using the Recurrence Plots approach. The systems studied there are a Schwarzschild black hole with a dipole magnetic field and a Kerr black hole immersed in a uniform axisymmetric magnetic field. It was found that the off-equatorial motion is regular until the particle energy is raised to the level at which trans-equatorial motion occurs. It was also concluded that the effect of black hole's rotation on the chaoticness is more involved than what was thought before.

1.4 This Work

In addition to the fact that astrophysical black holes are magnetized, they are rapidly rotating. Even slowly rotating black holes can be spun up by matter accretion [34, 35]. The spinning process is thought to be limited by $a = 0.998M$ due to the counteracting torque resulting from the absorption of the radiation from the disk [36]. Recent observational measurements of various black holes spins concluded that astrophysical black holes are

indeed rapidly rotating [37, 38, 39, 40].

The physics behind the bipolar jets associated with compact objects, in particular, active galactic nuclei is still an urging mystery. There have been several jet launching and collimation mechanisms proposed. It is noteworthy that a magnetic field is an essential ingredient in many of them. Nowadays, the most commonly discussed models are the gravito-hydromagnetic models which are studied via advanced computer simulations (see the references in the recent textbook [5]). It is unknown whether jets are powered by the accretion disk or the black hole's rotational energy. Recent observations concluded that the jets power is proportional to the black hole's spin [41, 42], in agreement with the mechanisms proposed by Blandford and Znajek [43]. The observations are congruent with computer simulations of gravitohydromagnetics of plasma accreting into rotating black holes, e.g. [44, 45, 46]. It should be noted, however, that a previous observation found no evidence for black hole rotation powering the jets in X-ray binaries [47].

In this thesis we consider a simplified and yet interesting model that may shed light on the high energy emissions associated with astrophysical black holes. The system we study consists of a charged particle in an equatorial circular orbit around Schwarzschild and Kerr black holes immersed in a weak uniform axisymmetric magnetic field. The magnetic field is normal to the orbital plane.

We then give the particle a kick off the orbit and observe how its dynamics evolves and whether it escapes or ends up captured by the black hole. In real situations the kick could be given for example by another particle or photon. To reduce the complexity of the problem we will consider only kicks that give the particle a velocity $v_{\perp}$ normal to the orbit, while keeping the azimuthal angular momentum unchanged.

The main effect of the magnetic field on the circular orbits of charged particles is bringing the ISCOs closer to the black hole event horizon. Negatively 'superbound' anti-Larmor retrograde stable circular orbits appear if the magnetic force is large enough (see Ch. 3). The inclusion of the magnetic field breaks down the constant of motion associated with the

Kerr spacetime hidden symmetry, the Carter constant (or simply the total angular momentum when the black hole is not rotating). Consequently, the equations of motion become non-integrable in general and numerical integration is required. Depending on the initial conditions and the parameters of the dynamical system, the motion can be chaotic as mentioned above.

The problem in the background of a Schwarzschild black hole is the subject of Ch. 2. The generalization of the problem when the black hole is rotating is the subject of Ch. 3.

Chapter 2 is based on the peer reviewed paper:
A. Al Zahrani *et al.*, "Critical Escape Velocity for a Charged Particle Moving around a Weakly Magnetized Schwarzschild Black Hole". *Phys. Rev. D* **87**, 084043 (2013).
Chapter 3 is based on the paper (in progress):
A. Al Zahrani, "Escape of Charged Particles Moving around a Weakly Magnetized Kerr Black Hole".

1.5 Appendix

The function $H(r,\theta)$ in the magnetized Kerr-Newman metric Eq. (1.3) is as follows:

$$H = 1 + \frac{H_{(1)}B + H_{(2)}B^2 + H_{(3)}B^3 + H_{(4)}B^4}{R^2}, \tag{1.6}$$

$$H_{(1)} = 2aQr\sin^2\theta, \tag{1.7}$$

$$H_{(2)} = \frac{1}{2}[(r^2+a^2)^2 - a^2\Delta\sin^2\theta]\sin^2\theta + \frac{3}{2}Q(a^2 + r^2\cos^2\theta), \tag{1.8}$$

$$\begin{aligned} H_{(3)} &= -\frac{Qa\Delta}{2r}[r^2(3-cos^2\theta)\cos^2\theta + a^2(1+\cos^2\theta)] \\ &+ \frac{aQ(r^2+a^2)^2(1+\cos^2\theta)}{2r} + \frac{Q^2a[(2r^2+a^2)\cos^2\theta + a^2]}{2r}, \end{aligned} \tag{1.9}$$

$$\begin{aligned} H_{(4)} &= \frac{1}{16}(r^2+a^2)^2R^2\sin^4\theta + \frac{1}{4}Ma^2r(r^2+a^2)\sin^6\theta \\ &+ \frac{1}{4}Ma^2Q^2r(\cos^2\theta - 5)\sin^2\theta\cos^2\theta \\ &+ \frac{1}{4}M^2a^2[r^2(\cos^2\theta - 3)^2\cos^2\theta + a^2(1+\cos^2\theta)^2] \\ &+ \frac{1}{8}Q^2(r^2+a^2)(r^2+a^2+a^2\sin^2\theta)\sin^2\theta\cos^2\theta \\ &+ \frac{1}{16}Q^4[r^2\cos^2\theta + a^2(1+\sin^2\theta)^2]\cos^2\theta. \end{aligned} \tag{1.10}$$

The expression for $\omega(r,\theta)$ reads:

$$\omega = \frac{(2Mr - Q^2)a\omega_{(1)}B + \omega_{(2)}B^2 + \omega_{(3)}B^3 + \omega_{(4)}B^4}{\Sigma}, \tag{1.11}$$

$$\omega_{(1)} = -2Qr(r^2+a^2), \tag{1.12}$$

$$\omega_{(2)} = -\frac{3}{2}aQ^2(r^2+a^2+\Delta\cos^2\theta), \tag{1.13}$$

$$\begin{aligned} \omega_{(3)} &= 4QM^2a^2r + \frac{1}{2}Qr(r^2+a^2)[r^2 - a^2 + (r^2+3a^2)\cos^2\theta] \\ &+ \frac{1}{2}Q^3r[(r^2+3a^2)\cos^2\theta - 2a^2] - 2Ma^2Q^3 \\ &+ QM[r^4 - a^4 + r^2(r+3a^2)\sin^2\theta], \end{aligned} \tag{1.14}$$

$$\begin{aligned}
\omega_{(4)} &= \frac{1}{2}a^3M^3r(3+\cos^4\theta) - \frac{1}{16}aQ^6\cos^4\theta \\
&- \frac{1}{8}aQ^4[r^2(2+\sin^2\theta)\cos^2\theta + a^2(1+\cos^4\theta)] \\
&+ \frac{1}{16}aQ^2(r^2+a^2)[r^2(1-6\cos^2\theta+3\cos^4\theta) - a^2(1+\cos^4\theta)] \\
&- \frac{1}{4}a^3M^2Q^2(3+\cos^4\theta) + \frac{1}{4}aM^2[r^4(3-6\cos^2\theta+\cos^4\theta) \\
&+ 2a^2r^2(3\sin^2\theta - 2\cos^4\theta) - a^4(1+\cos^4\theta)] \\
&+ \frac{1}{8}aMQ^4r\cos^4\theta + \frac{1}{4}aMQ^2r[2r^2(3-\cos^2\theta)\cos^2\theta \\
&- a^2(1-3\cos^2\theta-2\cos^4\theta)] \\
&+ \frac{1}{8}aMr(r^2+a^2)[r^2(3+6\cos^2\theta-\cos^4\theta) \\
&- a^2(1-6\cos^2\theta-3\theta^4\theta)]. \qquad (1.15)
\end{aligned}$$

The vector potential generating the electromagnetic fields is

$$A_\mu = (\Phi_0 - \omega\Phi_3, 0, 0, \Phi_3). \qquad (1.16)$$

Φ_0 is given as

$$\Phi_0 = \frac{\Phi_0^{(0)} + \Phi_0^{(1)}B + \Phi_0^{(2)}B^2 + \Phi_0^{(3)}B^3}{4\Sigma}, \qquad (1.17)$$

where

$$\Phi_0^{(0)} = 4[-Qr(r^2+a^2)], \qquad (1.18)$$

$$\Phi_0^{(1)} = -6aQ^2(r^2+a^2+\Delta\cos^2\theta), \qquad (1.19)$$

$$\begin{aligned}
\Phi_0^{(2)} &= -3Q\{(r+2M)a^4 - (r^2+4Mr+\Delta\cos^2\theta)r^3 \\
&+ a^2[2Q^2(r+2M) - 6Mr^2 - 8M^2r - 3\Delta r\cos^2\theta]\}, \qquad (1.20)
\end{aligned}$$

$$\begin{aligned}\Phi_0^{(3)} &= -\frac{1}{2}a\{4a^4M^2+(a^4+12a^2M^2)Q^2+2a^2Q^4+2a^4Mr \\ &- 24a^2M^3r+4a^2Mq^2r-24a^2M^2r^2-4a^2Mr^3-12M^2r^4 \\ &- Q^2r^4-6Mr^5-6r\Delta[2M(r^2+a^2)-Q^2r]\cos^2\theta \\ &+ \Delta[Q^4-3Q^2r^2+2Mr^3+a^2(4M^2-Q^2-6Mr)]\cos^4\theta\}. \quad (1.21)\end{aligned}$$

Φ_3 reads

$$\Phi_3 = \frac{\Phi_3^{(0)}+\Phi_3^{(1)}B+\Phi_3^{(2)}B^2+\Phi_3^{(3)}B^3}{R^2H}, \quad (1.22)$$

where

$$\Phi_3^{(0)} = aQr\sin^2\theta, \quad (1.23)$$

$$\Phi_3^{(1)} = \frac{1}{2}[\Sigma\sin^2\theta+3Q^2(a^2+r^2\cos^2\theta)], \quad (1.24)$$

$$\begin{aligned}\Phi_3^{(2)} &= \frac{3}{4}aQr(r^2+a^2)\sin^4\theta+\frac{3}{2}aQM[r^2(3-\cos^2\theta)\cos^2\theta \\ &+ a^2(1+\cos^2\theta)]-\frac{3}{4}aQ^3r\sin^2\theta\cos^2\theta, \quad (1.25)\end{aligned}$$

$$\begin{aligned}\Phi_3^{(3)} &= \frac{1}{8}R^2(r^2+a^2)^2\sin^4\theta+\frac{1}{2}a^2Mr(r^2+a^2)\sin^6\theta \\ &- \frac{1}{2}a^2Q^2Mr(5-\cos^2\theta)\sin^2\theta\cos^2\theta \\ &+ \frac{1}{2}a^2M^2[r^2(3-\cos^2\theta)^2\cos^2\theta+a^2(1+\cos^2\theta)^2] \\ &+ \frac{1}{4}Q^2(r^2+a^2)[r^2+a^2(1+\sin^2\theta)]\sin^2\theta\cos^2\theta \\ &+ \frac{1}{8}Q^4[r^2\cos^2\theta+a^2(2-\cos^2\theta)^2]\cos^2\theta. \quad (1.26)\end{aligned}$$

Bibliography

[1] D. Grasso, H. Rubinstein, *Phys Reports* **348**, 163 (2001).

[2] M. Shibata and K. Taniguchi, *Living Rev. Relativity*, **14** (2011), 6.

[3] C. Kouveliotou et al., *Nature*, **393**, 235 (1998).

[4] A. Ibrahim et al., *ApJ*, **574**, L51 (2002).

[5] G. Romero and G. Vila, *Introduction to Black Hole Astrophysics* (Springer-Verlag, Berlin, 2013).

[6] B. Punsly, *Black Hole Gravitohydromagnetics*, 2nd Edition (Springer-Verlag, Berlin, 2008).

[7] N. Silant'ev, Y. Gnedin, S. Buliga, M. Piotrovich and T. Natsvlishvili, arXiv:1203.2763 (2012).

[8] M. Piotrovich, N. Silant'ev, Y. Gnedin, and T. Natsvlishvili, arXiv:1002.4948 (2010).

[9] M. Camenzind, *Compact Objects in Astrophysics: White Dwarfs, Neutron Stars and Black Holes* (Springer-Verlag, Berlin, 2013).

[10] J. Miller et al, *Nature* **441**, 22 (2006).

[11] F. Ernst, *J. Math. Phys.* **17**, 54 (1976).

[12] M. Melvin, *Phys. Lett.* **8**, 65 (1964).

[13] F. Ernst and W. Wild, *J. Math. Phys.* **17**, 182 (1976).

[14] G. Gibbons, A. Mujtaba and C. Pope, arXiv:1301.3927v2 (2013).

[15] E. Esteban *Journal of Physics: Conference Series* **189**, 012012 (2009).

[16] G. Gibbons, Y. Pang and C. Pope, arXiv:1310.3286 (2013).

[17] R. Wald, *Phys. Rev. D* **10**, 1680 (1974).

[18] K. Kokkots, R. Konoplya and A. Zhidenko, *Phys. Rev. D* **83**, 024031 (2011).

[19] J. Bičák and L. Dvořák, *Gen Relativ Gravit* **7**, 959 (1976).

[20] O. Kopáček, *WDS'08 Proceedings of Contributed Papers* Part III, 198 (2008).

[21] J. Pettterson, *Phys. Rev. D* **10**, 3166 (1974).

[22] J. Bičák and L. Dvořák, *Czech. J. Phys. B* **27**, 127 (1977).

[23] J. Bičák and L. Dvořák, *Phys. Rev. D* **22**, 2933 (1980).

[24] N. Dadhich, C. Hoenselaers and C Vishveshwara, *J. Phys. A: Math. Gen.* **12**, 2 (1979).

[25] A. Prasanna and R. Varma , *Pramana* **8**, 229 (1977).

[26] A. Prasanna and C. Vishveshwara, *Pramana* **11**, 359 (1978).

[27] A. N. Aliev and N. Özdemir, Mon. Not. Roy. Astron. Soc. **336**, 241 (2002).

[28] A. Prasanna and S. Sengupta, *Phys. Lett. A* **193**, 25 (1994).

[29] V. Karas and D. Vokrouhlicky, *Gen. Relativ. Gravit.* **24**, 729 (1992).

[30] Y. Nakamura and T. Ishizuka, *Astrophys. Space Sci.* **210**, 105 (1993).

[31] M. Santoprete and G. Cicogna, *Gen. Relativ. Gravit.* **34**, 1107 (2002).

[32] M. Takahashi and H. Koyama, *Astrophys. J.* **693**, 472 (2009).

[33] O. Kopacek, V. Karas, J. Kovar, and Z. Stuchik, *Astrophys. J.* **722**, 1240 (2010).

[34] J. M. Bardeen, Nature **226**, 64 (1970).

[35] D. Lynden-Bell Nature **223**, 690 (1969).

[36] K. S. Thorne Astrophys. J. **191**, 507 (1974).

[37] L. Brenneman, *Measuring the Angular Momentum of Supermassive Black Holes* (Springer Briefs in Astronomy, 2013).

[38] J. E. McClintock, R. Narayan, and J. F. Steiner, arXiv:1303.1583v2 (2013).

[39] C. S. Reynolds, arXiv:1302.3260v2 (2013).

[40] J. E. McClintock, R. Narayan, L. Gou, J. Liu, R. F. Penna, and J. F. Steiner, *AIP Conf. Proc.* **1248**, 101 (2010).

[41] R. Narayan, J. McClintock, *Mon. Not. R. Astron. Soc.* **419**, L69 (2012).

[42] R. Narayan, J. McClintock and A. Tchekhovskoy, arXiv:1303.3004v1 (2013).

[43] R. D. Blandford, R. L. Znajek, *Mon. Not. Roy. Astron. Soc.* **179**, 433 (1977).

[44] S. Koide, K. Shibata, T. Kudoh and D. Meier, *Science*, **295**, 1688 (2002).

[45] V. Semenov, S. Dyadechkin and B. Punsly, Science, **305**, 978 (2004).

[46] A. Tchekhovskoy, J. McKinney and R. Narayan, *Journal of Physics: Conference Series* **372**, 012040 (2012).

[47] R. Fender, E. Gallo and D. Russell, *Mon. Not. R. Astron. Soc.* **406**, 1425 (2010).

Chapter 2

Escape of Charged Particles Moving around a Weakly Magnetized Schwarzschild Black Hole

2.1 Introduction

In this chapter it is demonstrated that charged-particle motion near a weakly magnetized Schwarzschild black hole is generically chaotic. The critical escape velocity required for such a particle to escape to infinity is found, and some properties of the near-critical motion are discussed. In Sec. 2.2 the model used is discussed and an expression for the escape velocity for a neutral particle is presented. The Wald magnetization procedure is introduced in Sec. 2.3. In Sec. 2.4 the equations of motion of a charged particle moving around a weakly magnetized Schwarzschild black hole are written. A dimensionless form of the equations and the initial conditions for the particle's motion are given in Sec. 2.5. In Sec. 2.6 several examples of qualitatively different orbits of a charged particle near the weakly magnetized black hole are given. The basin of attraction method is applied for an analysis of the charged-particle motion in

Sec. 2.7. There the chaotic properties of the trajectories are demonstrated and the fractal dimensions in the proper domains are determined. The chapter is concluded with a brief summary of results in Sec. 2.8.

2.2 Escape Velocity of a Neutral Particle

Before considering the escape-velocity problem for a charged particle in a weakly magnetized black hole, let us recall the well-known results for a similar problem in the simpler case when a particle is neutral and the magnetic field is absent. The background Schwarzschild metric is

$$ds^2 = -f dt^2 + f^{-1} dr^2 + r^2 d\omega^2, \tag{2.1}$$

$$d\omega^2 = d\theta^2 + \sin^2\theta d\phi^2, \quad f = 1 - \frac{r_g}{r}. \tag{2.2}$$

Here $r_g = 2GM$ is the gravitational radius of the black hole. There exist three commuting integrals of motion. Two of them are generated by the Killing vectors

$$\xi^\mu_{(t)} = \delta^\mu_t, \;\; \xi^\mu_{(\phi)} = \delta^\mu_\phi, \tag{2.3}$$

reflecting invariance with respect to time translations and rotations around the symmetry axis. The corresponding conserved quantities are the specific energy $\mathcal{E}$ and the specific azimuthal angular momentum $\mathcal{L}$,

$$\mathcal{E} \equiv -p_\mu \xi^\mu_{(t)}/m = \dot{t} f, \tag{2.4}$$

$$\mathcal{L} \equiv p_\mu \xi^\mu_{(\phi)}/m = \dot{\phi} r^2 \sin^2\theta. \tag{2.5}$$

Here m is the mass of the particle, and u^μ and $p^\mu = m u^\mu$ are its four-velocity and four-momentum, respectively. Here and in what follows, the overdot denotes the derivative with respect to the proper time. The third integral of motion is the square of the specific total angular momentum,

$$\mathcal{J}^2 \equiv r^4 \dot{\theta}^2 + \frac{\mathcal{L}^2}{\sin^2\theta} = r^2 v_\perp^2 + \mathcal{L}^2. \tag{2.6}$$

Here $v_{_\perp}$ denotes the following quantity:

$$v_{_\perp} \equiv -r\dot{\theta}_k. \tag{2.7}$$

where $\dot{\theta}_k$ is the initial polar angular velocity of the particle. Using the normalization condition $u^\mu u_\mu = -1$ one obtains

$$\dot{r}^2 = \mathcal{E}^2 - U, \quad U = f(1 + \mathcal{J}^2/r^2). \tag{2.8}$$

The motion of the particle is planar. We let this plane coincide with the equatorial plane. Then $\dot{\theta} = 0$ and the effective potential for the radial motion takes the form

$$U = \tilde{U} \equiv f(1 + \mathcal{L}^2/r^2). \tag{2.9}$$

Consider a particle at the circular orbit $r = r_o$, where r_o corresponds to the local minimum of the effective potential $\tilde{U}$. This orbit exists for $r_o \in (3r_g, \infty)$. The corresponding specific energy and azimuthal angular momentum are

$$\mathcal{E}_o = \frac{\sqrt{2}(r_o - r_g)}{\sqrt{r_o(2r_o - 3r_g)}}, \quad |\mathcal{L}_o| = \frac{r_o\sqrt{r_g}}{\sqrt{2r_o - 3r_g}}. \tag{2.10}$$

The ISCO is defined by $r_o = 3r_g$, which corresponds to an inflection point of the effective potential where $\partial_r^2\tilde{U} = \partial_r\tilde{U} = 0$. For the ISCO we have $\mathcal{E}_{\rm ISCO} = 2\sqrt{2}/3 \approx 0.943$ and $|\mathcal{L}_{\rm ISCO}| = r_g\sqrt{3}$.

Suppose now that the particle in a circular orbit collides with another particle or photon, so that after the collision it will move within a new plane tilted with respect to the original equatorial plane. In a general case, all three types of its motion are possible: (i) bounded motion, (ii) escape to infinity, and (iii) capture by the black hole. The result certainly depends on the details of the collision mechanism. For small values of the transferred energy and momentum the orbit will be only slightly perturbed. However, for larger values of $\mathcal{E} - \mathcal{E}_o$ the particle can go away from the initial plane, and finally be captured by the black hole or escape

to infinity.

In a general case, as a result of the collision the particle will have new integrals of motion: $\mathcal{E}$, $\mathcal{L}$ and $\mathcal{J}^2$. For the case of a neutral particle in the Schwarzschild black hole one can easily obtain the conditions of escape in an analytical form. To be able to obtain results which allow a rather simple analysis and presentation we simplify the problem and reduce the space of initial data by imposing the following restrictions: (i) the azimuthal angular momentum is not changed, and (ii) the initial radial velocity after the collision remains the same. Under these restrictions there exists only one parameter that determines the motion of the particle, namely the new value of its energy. Under these conditions, as a result of the collision the particle acquires a velocity $v_{_\perp}$ in the direction orthogonal to the equatorial plane [see Eq. (2.7)].

After the collision, the total angular momentum and the energy of the particle are

$$\mathcal{J}^2 = r_o^2 v_{_\perp}^2 + \mathcal{L}^2, \tag{2.11}$$

$$\mathcal{E} = \sqrt{\mathcal{E}_o^2 + v_{_\perp}^2 (r_o - r_g)/r_o}. \tag{2.12}$$

As a result of the collision, the total angular momentum of the particle changes from its original value $\mathcal{L}^2$ to $\mathcal{J}^2$, given by Eq. (2.11). The effective potential U defined by the new value of $\mathcal{J}^2$ is greater than that before the collision. Moreover, the particle always accelerates away from the black hole since

$$U'(r_o) = -\frac{(2r_o - 3r_g)}{r_o^2} v_{_\perp}^2, \tag{2.13}$$

is always negative outside the photon sphere given by $r_o = \frac{3}{2} r_g$. The particle is therefore to the right of the single maximum of U and will not experience any turning point and escape to infinity if $\mathcal{E} \geq 1$, or

$$|v_{_\perp}| \geq \sqrt{\frac{r_o(1 - \mathcal{E}_o^2)}{(r_o - r_g)}}. \tag{2.14}$$

In particular, for the ISCO we have the escape condition $v_{_\perp}^{esc} \geq 1/\sqrt{6}$,

where the equality corresponds to $\mathcal{E} = 1$.

The black hole metric (2.1) has the evident discrete symmetries

$$\phi \to -\phi, \qquad \theta \to \pi - \theta, \tag{2.15}$$

which imply the symmetry of the problem with respect to the transformations

$$\mathcal{L} \to -\mathcal{L}, \qquad v_{\perp} \to -v_{\perp}. \tag{2.16}$$

2.3 Weakly Magnetized Black Holes

We follow the magnetization procedure introduced by Wald [1]. In a Ricci flat spacetime a Killing vector ξ^{μ} obeys the equation

$$\xi^{\mu}{}_{;\nu}{}^{;\nu} = 0. \tag{2.17}$$

This is identical to the source-free Maxwell equations for a four-potential A^{μ} in the Lorentz Gauge ($A^{\mu}{}_{;\mu} = 0$),

$$A^{\mu}{}_{;\nu}{}^{;\nu} = 0. \tag{2.18}$$

Therefore, any linear combination of the Killing vectors the spacetime admits will serve as a solution to the Maxwell equations in that Ricci flat spacetime. It should be mentioned that the corresponding electromagnetic field is assumed to be too weak to modify the spacetime geometry. The choice

$$A^{\mu} = \frac{B}{2}\xi^{\mu}_{(\phi)}, \tag{2.19}$$

corresponds to a uniform axisymmetric magnetic field that has strength B asymptotically [1, 2, 3][1]. It is this potential that will be used in this thesis. In what follow we will refer to this choice as the electromagnetic potential or simply A^{μ}.

[1]The choice $A^{\mu} = -\frac{Q}{2M}\xi^{\mu}_{(t)}$ corresponds to a weakly charged black hole with a charge $Q \ll M$.

The dynamics of a charged particle of mass m and charge q in an electromagnetic field in a curved spacetime is governed by the equation

$$m\frac{du^\mu}{d\tau} = qF^\mu_{\ \nu}u^\nu, \tag{2.20}$$

where $F^\mu_{\ \nu}$ is the electromagnetic field tensor given by

$$F_{\mu\nu} = A_{\nu,\mu} - A_{\mu,\nu}. \tag{2.21}$$

The generalized four-momentum of the particle is

$$P^\mu = mu^\mu + qA^\mu. \tag{2.22}$$

In the frame of an observer with four-velocity u^μ, the electric and magnetic fields are, respectively

$$E^\mu = F^{\mu\nu}u_\nu, \tag{2.23}$$

$$B^\mu = -\frac{1}{2}\frac{\varepsilon^{\mu\nu\lambda\sigma}}{\sqrt{-g}}F_{\lambda\sigma}u_\nu, \tag{2.24}$$

where g is the determinant of the spacetime metric and $\varepsilon_{\mu\nu\lambda\sigma}$ is $+1$ (-1) for even (odd) permutations of 0123 and 0 otherwise.

The weak field approximation breaks down when the magnetic field creates curvature comparable to that made by the black hole mass. We therefore write

$$B^2 \sim M^{-2}, \tag{2.25}$$

In Gaussian units, the Wald approximation breaks down when

$$B \sim \frac{c^4}{G^{3/2}M}\,(\text{gauss}). \tag{2.26}$$

For solar mass black holes one gets $B \sim 10^{19}$ gauss! The typical magnetic field strength near a black hole horizon has been estimated to be $\sim 10^8$ gauss (or $10^{-15}\,\text{meter}^{-1}$) for stellar mass black holes and $\sim 10^4$ gauss (or $10^{-19}\,\text{meter}^{-1}$) for supermassive black holes [4, 5]. These es-

timates validate ignoring corrections to the metric due to the presence of the magnetic field. Despite that B is tiny its effect on the dynamics is significant since the charge-to-mass ratio $q/m = 2.04 \times 10^{21}(1.11 \times 10^{18})$ for electrons (protons). For electrons (protons) near a typical stellar mass black hole $\frac{qB}{m} \sim 10^7\ (10^3)$ meter^{-1} and near typical a supermassive black hole $\frac{qB}{m} \sim 10^3\ (10^{-1})$ meter^{-1}.

2.4 Charged Particles near a Magnetized Black Hole

The specific energy and azimuthal angular momentum of the particle are constants of motion since the electromagnetic potential is compatible with the temporal and azimuthal Killing vectors. We therefore write

$$\mathcal{E} \equiv -\xi^{\mu}_{(t)} P_{\mu}/m = \dot{t} f, \tag{2.27}$$

$$\mathcal{L} \equiv \xi^{\mu}_{(\phi)} P_{\mu}/m = (\dot{\phi} + b)\, r^2 \sin^2\theta. \tag{2.28}$$

where $b \equiv \frac{qB}{2m}$. Solving for $\dot{t}$ and $\dot{\phi}$ we get

$$\dot{t} = f^{-1}\mathcal{E}\,, \quad \dot{\phi} = \frac{\mathcal{L}}{r^2 \sin^2\theta} - b. \tag{2.29}$$

The ρ and θ components of Eq. (2.20) read, respectively,

$$\begin{aligned} \ddot{r} &= \frac{1}{2}(2r - 3r_g)\left(\dot{\theta}^2 + \frac{\mathcal{L}^2}{r^4 \sin^2\theta}\right) + \frac{r_g(2\mathcal{L}b - 1)}{2r^2} \\ &- \frac{b^2}{2}(2r - r_g)\sin^2\theta, \end{aligned} \tag{2.30}$$

$$\ddot{\theta} = -\frac{2}{r}\dot{r}\dot{\theta} + \frac{\mathcal{L}^2 \cos\theta}{r^4 \sin^3\theta} - b^2 \sin\theta\cos\theta. \tag{2.31}$$

The normalization of the four-velocity $u_{\mu}u^{\mu} = -1$ gives the following

first-order equation

$$\mathcal{E}^2 = \dot{r}^2 + r^2 f \dot{\theta}^2 + U_{\text{eff}}, \tag{2.32}$$

$$U_{\text{eff}} = f\left[1 + r^2 \sin^2\theta \left(\frac{\mathcal{L}}{r^2 \sin^2\theta} - b\right)^2\right]. \tag{2.33}$$

This equation is a constraint. If it is satisfied at the initial moment of time, then it is always valid, provided that the dynamics of $r(\tau)$ and $\theta(\tau)$ is controlled by Eqs. (2.30) and (2.31).

From Eqs. (2.30)–(2.33) we can see that there are two dynamically different modes of radial motion, depending on whether $\mathcal{L}b > 0$ or $\mathcal{L}b < 0$. In the equatorial plane, the Lorentz force is radially outward (inward) when $\mathcal{L}b > 0$ ($\mathcal{L}b < 0$). In this chapter we choose to keep $b > 0$ and let $\mathcal{L}$ take both signs to consider all dynamically distinct cases.

The dynamics is invariant under reflection with respect to the equatorial plane or

$$\theta \to \pi - \theta, \qquad \dot{\theta} \to -\dot{\theta}. \tag{2.34}$$

This makes it possible to keep $v_\perp > 0$ without loss of generality.

2.5 Dimensionless Form of the Equations

In order to study charged particles escape we need to integrate the equation of motion numerically. For convenience, we rewrite them in a dimensionless form. Let us define the dimensionless quantities

$$\sigma = \frac{\tau}{r_g}, \quad \rho = \frac{r}{r_g}, \quad \ell = \frac{\mathcal{L}}{r_g}, \quad \beta = b r_g. \tag{2.35}$$

Equations (2.30)–(2.33) recast in the dimensionless form read

$$\begin{aligned}\frac{d^2\rho}{d\sigma^2} &= \frac{1}{2}(2\rho-3)\left(\frac{d\theta}{d\sigma}\right)^2+\frac{(2\ell\beta-1)}{2\rho^2}+\frac{\ell^2(2\rho-3)}{2\rho^4\sin^2\theta}\\ &- \frac{\beta^2}{2}(2\rho-1)\sin^2\theta, \qquad (2.36)\\ \frac{d^2\theta}{d\sigma^2} &= -\frac{2}{\rho}\frac{d\rho}{d\sigma}\frac{d\theta}{d\sigma}+\frac{\ell^2\cos\theta}{\rho^4\sin^3\theta}-\beta^2\sin\theta\cos\theta. \qquad (2.37)\\ \mathcal{E}^2 &= \left(\frac{d\rho}{d\sigma}\right)^2+\rho(\rho-1)\left(\frac{d\theta}{d\sigma}\right)^2+U_{\rm eff}, \qquad (2.38)\\ U_{\rm eff} &= \left(1-\frac{1}{\rho}\right)\left[1+\frac{(\ell-\beta\rho^2\sin^2\theta)^2}{\rho^2\sin^2\theta}\right]. \qquad (2.39)\end{aligned}$$

In an equatorial circular orbit of radius ρ_o the particle energy is

$$\mathcal{E}_o=\left(1-\frac{1}{\rho_o}\right)^{1/2}\left[1+\frac{(\ell-\beta\rho_o^2)^2}{\rho_o^2}\right]^{1/2}. \qquad (2.40)$$

After the kick, the particle acquires a polar velocity $v_\perp>0$ and its energy changes to

$$\mathcal{E}=\left[\mathcal{E}_o^2+\frac{(\rho_o-1)}{\rho_o}v_\perp^2\right]^{1/2}. \qquad (2.41)$$

The azimuthal angular momentum of the particle ℓ will be kept constant as mentioned above. For brevity, we will take the initial circular orbit to be an ISCO. The parameters ℓ and β for an ISCO—in terms of the orbit radius ρ_o—are obtained by solving $U'_{\rm eff}=U''_{\rm eff}=0$ with $\theta=\pi/2$ for these parameters. The expressions read

$$\ell=\pm\frac{\rho_o}{\sqrt{2}}\frac{\sqrt{3\rho_o-1}}{\sqrt{(4\rho_o-9)\rho_o\pm\sqrt{3\rho_o-1}\sqrt{3-\rho_o}+3}} \qquad (2.42)$$

$$\beta=\frac{1}{\sqrt{2}\rho_o}\frac{\sqrt{\rho_o-3}}{\sqrt{(4\rho_o-9)\rho_o\pm\sqrt{3\rho_o-1}\sqrt{3-\rho_o}+3}} \qquad (2.43)$$

When $\rho_0 = 3$, $\beta = 0$ as expected. For very large β, the radius of the ISCO approaches $\rho_o = 1$ for $\ell > 0$ and $\rho_o = (5 + \sqrt{13})/4$ for $\ell < 0$.

2.6 Types of the Trajectories

Given the orbit radius $\rho = \rho_o$ and the energy $\mathcal{E} > \mathcal{E}_o$ of the particle after the kick, we integrate the dynamical equations (2.36) and (2.37) numerically. The numerical integration yields the trajectory corresponding to the given initial conditions. The dynamical equations were solved using the built-in *MATHEMATICA* 8.0 function NDSOLVE. The integral of motion of the system $\mathcal{E}$ [see Eqs. (2.38) and (2.41)] was used to estimate the accuracy of the numerical solver. For our calculations the energy error $|\Delta\mathcal{E}|$ was found to be less than 10^{-6}.

The results of the numerical integration show that there are three different types of final motion for the particle:

1. The particle is captured by the black hole.

2. The particle escapes to $z \to +\infty$.

3. The particle escapes to $z \to -\infty$.

The outcome of the motion is considered a capture when ρ reaches 1. It is considered an escape if $|z|$ reaches 10^3. In most cases at least, the specific gravitational potential there is much smaller than v_z^2, where v_z is z-component of the particle's velocity. The maximum computation time was chosen as $\sigma = 10^5$. In escape cases, it was found that the cumulative error $|\Delta\mathcal{E}|$ can reach 10^{-2}. The accuracy of the numerical solver can be increased to achieve much better accuracy. While increasing the accuracy is not a problem when only a few trajectories are to be generated, it can increase the computation time greatly when the equations of motions are integrated hundreds of thousands of times, as in the case of producing the basins of attraction plots (see below). However, at least in the cases we have studied, increasing the accuracy of the numerical solver does not change the final state of the motion significantly.

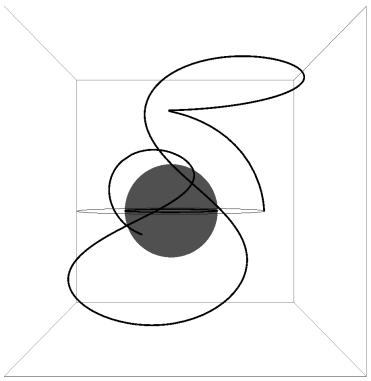

(**a**)

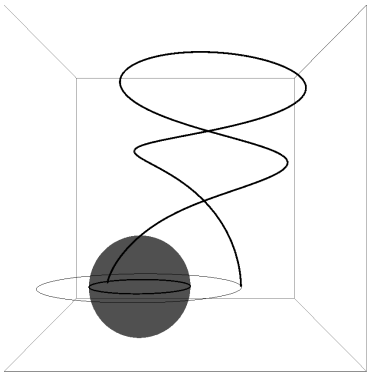

(**b**)

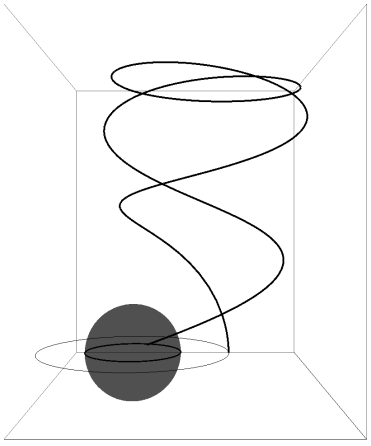

(**c**)

Figure 2.1: Examples of "capture" trajectories. In each case a charged particle is kicked up from its original ISCO at $\rho_o = 2$ for $\ell > 0$. The energy $\mathcal{E}$ after the kick is (a) 1.12 (b) 1.2 and (c) 1.3.

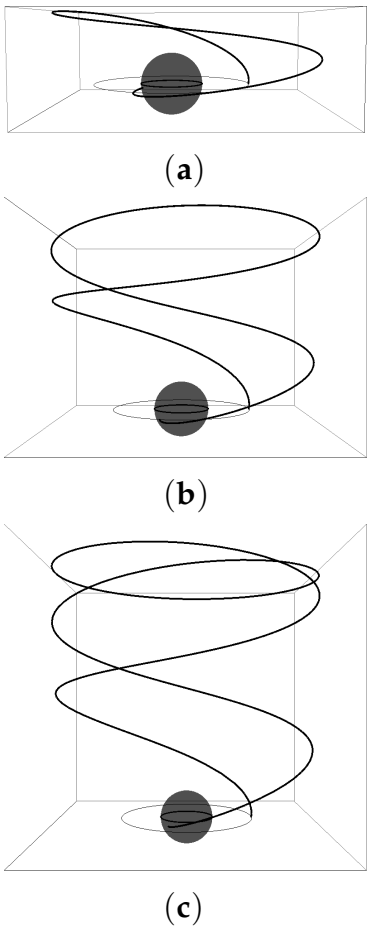

(**a**)

(**b**)

(**c**)

Figure 2.2: Examples of "capture" trajectories. In each case a charged particle is kicked up from its original ISCO at $\rho_o = 2.5$ for $\ell < 0$. The energy $\mathcal{E}$ after the kick is (**a**) 1.35 (**b**) 1.475 and (**c**) 1.525.

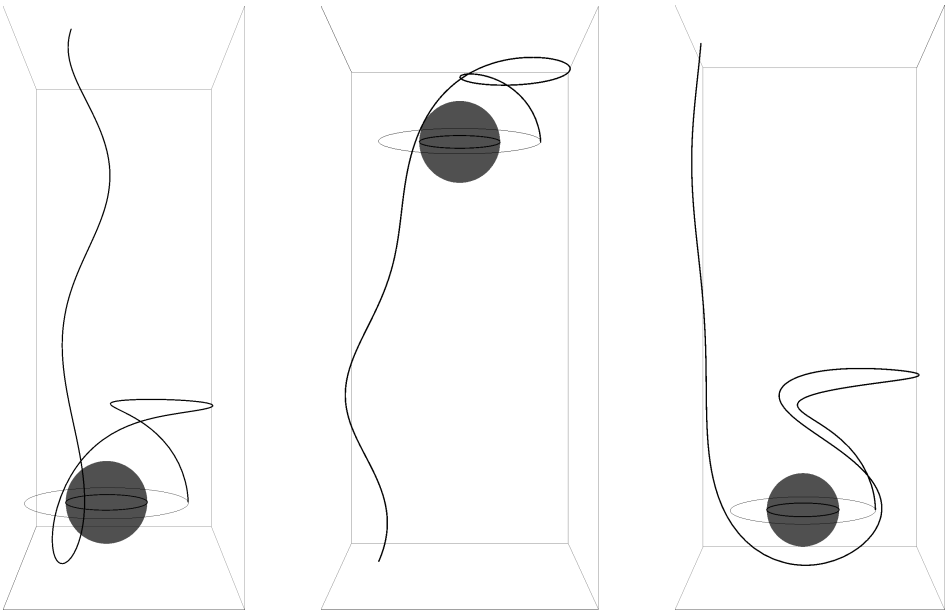

Figure 2.3: Examples of "escape" trajectories. In each case a charged particle is kicked up from its original ISCO at $\rho_o = 2$ for $\ell > 0$. The energy $\mathcal{E}$ after the kick is (a) 1.025 (b) 1.05 and (c) 1.135.

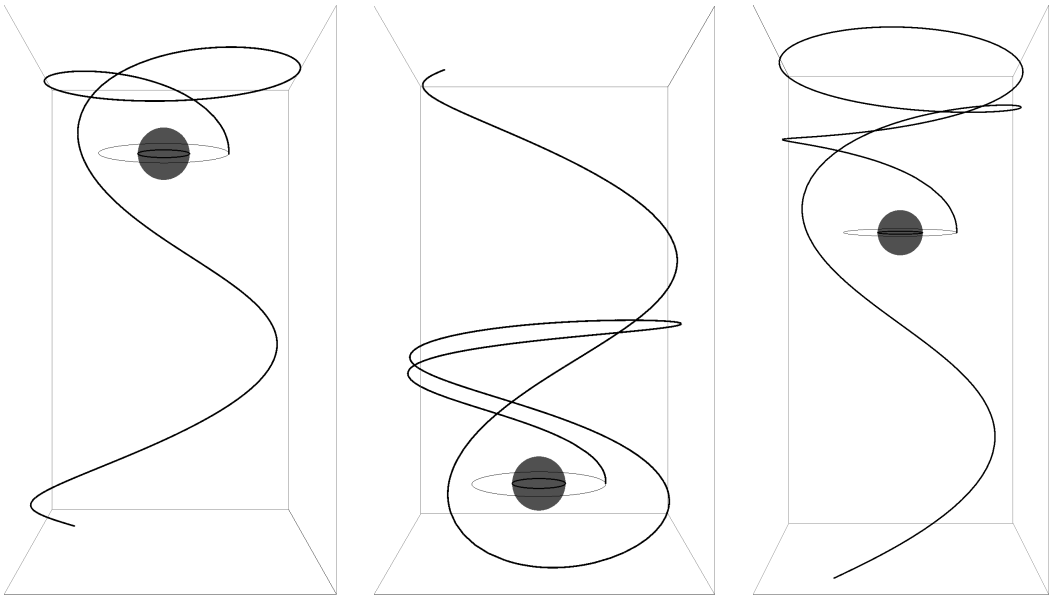

(**a**) (**b**) (**c**)

Figure 2.4: Examples of "escape" trajectories. In each case a charged particle is kicked up from its original ISCO at $\rho_o = 2.5$ for $\ell < 0$. The energy $\mathcal{E}$ after the kick is (a) 1.415 (b) 1.46 and (c) 1.5.

To distinguish the final states of the particle we introduce an integer number n. It takes the value 0 for the capture case and ± 1 for escape to $z \to \pm\infty$, respectively.

If one focuses on a single trajectory, one can see that there exists a variety of its type, each with qualitatively different behavior of the particle within the domain close to the black hole. For each of these types of motion the particle may pass through the equatorial plane a number of times. To characterize the dynamical behavior of the particle in this domain we introduce the "crossing" number c, which counts how many times the particle crosses the equatorial plane before it gets captured or escapes to the spatial infinity. For our choice of the initial conditions, the particle after the kick starts its motion from the equatorial plane in the positive z direction. For this reason, it is evident that for $n = +1$ the crossing number c is even, while for $n = -1$ it is odd. In particular, when a particle goes to $z \to +\infty$ without further crossing the equatorial plane, $c = 0$.

In rare cases of the computations the particle stays in the vicinity of the equatorial plane during the numerical lifetime σ. It crosses the plane many times and forms a compact cloud in the corresponding phase space.

Figures 2.1–2.4 illustrate possible "capture" and "escape" trajectories of the charged particle near the magnetized black hole for both the $\ell > 0$ at $\rho_o = 2$ and $\ell < 0$ at $\rho_o = 2.5$ cases. The figures collect several examples of such trajectories for different values of the invariants n and c.

The fate of a kicked particle was found to be extremely sensitive to the initial conditions; even a very tiny change of these conditions may drastically modify its global behavior. Such an extreme sensitivity is an indication of the nonintegrability of the system and its chaotic nature. It can be shown that the system is Hamiltonian and conservative. Chaos in Hamiltonian systems has been extensively studied (see, e.g., Ref. [6] and references therein). For an analysis of our dynamical system we shall use the methods developed for the study of chaotic dynamical systems that possess several coexisting final states.

In our system the particle is fated to be captured by the black hole, escape it up (down) and approach $z = \infty$ ($z = -\infty$) asymptotically, or end

up in an orbit "meta-stable" within the computation time. Keeping the possible meta-stable orbits aside, the system therefore has three *attractors*.

An attractor of a dynamical system is a subset of the set of all possible states of the system which an orbit with certain initial conditions approaches asymptotically [6]. The set of initial conditions that leads to an attractor is its *basin of attraction*. In our system, we have a charged particle at an ISCO around a magnetized black hole with fixed parameters M, and B. Therefore the space of initial conditions for the particle is the set $\{\rho_o, \mathcal{E}(\dot{\theta}_k)\}$. The boundary between different basins of attraction is a simple smooth curve in case of regular systems. In chaotic systems the basin boundary is a *fractal* boundary. A fractal is a geometrical object that has fractal dimension D_f larger than its topological dimension. A characteristic of fractals is the appearance of self-similar patterns at different magnifications.

2.7 Basin of Attraction Analysis

2.7.1 Basin of Attraction Plots

Here we use the basin of attraction approach for the analysis of the asymptotic behavior of the particle trajectories. The approach is well suited for non-compact scattering systems. This method, in particular, was used in the analysis of another dynamical system appearing in general relativity (see, e.g., Ref. [7]). The corresponding basins of attraction are presented in Fig. 2.5. As we mentioned, the particle is initially at the ISCO. Figure 2.5(a) corresponds to the case $\ell > 0$ and Fig. 2.5(b) to the case $\ell < 0$. The horizontal axis on these plots shows the dimensionless parameter ρ_o of the ISCO, while the vertical axis shows the dimensionless energy $\mathcal{E}$ of the particle after the kick. The white domains in these plots correspond to the region forbidden for the particle's ISCO. The colored regions in these plots consist of square pixels with a side size ρ and $\mathcal{E}$ equal to 2.5×10^{-3}. We used three different colors for these pixels. The color of a pixel determines the final outcome of the particle motion. These colors are chosen so

that red corresponds to the particle capture, green corresponds to escape to $z \to +\infty$ ($n = 1$), yellow corresponds to escape to $z \to -\infty$ ($n = -1$), and blue corresponds to meta-stable orbits.

2.7.2 Critical Escape Energy and Velocity

The general structure of the plots shown in Fig. 2.5 can be described as follows. The red region—which adjoins to the white region at the bottom of the plots—corresponds to the particle capture. The uniformly green region in the upper-right part of the plots corresponds to the particle's escape to $z \to +\infty$. The crossing number in this region is $c = 0$. This region is restricted from below by a diffuse domain. The uniform region is separated from the diffuse domain by a line which we call the critical-escape-energy line. Using our numerical results we can estimate the critical escape energy of the particle describing this line. The approximate empirical expression for the case $\ell > 0$ is

$$\mathcal{E}_{\text{esc}} \approx 1 + \frac{0.115(3.463 - \rho_o)}{(\rho_o - 1.851)(3.433 - \rho_o)}. \tag{2.44}$$

and for the case $\ell < 0$ is

$$\mathcal{E}_{\text{esc}} \approx 1 + \frac{0.4393(3.198 - \rho_o)}{(\rho_o - 2.105)(3.667 - \rho_o)}, \tag{2.45}$$

The maximal relative error of the escape energy in these expressions is 0.2%. Figures 2.6(a) and 2.6(b) illustrate the escape energy $\mathcal{E}_{\text{esc}}$ for the $\ell > 0$ and $\ell < 0$ cases, respectively.

Using these empirical expressions together with Eqs. (2.40)–(2.43) we can determine the critical escape velocity $v_{\perp}^{esc}$ as a function of ρ_o. Figures 2.7(a) and 2.7(b) illustrate the critical escape velocity for $\ell > 0$ and $\ell < 0$, respectively.

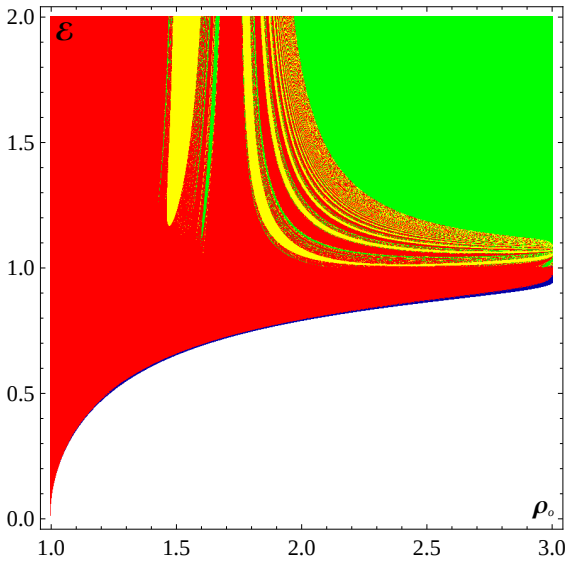

(**a**)

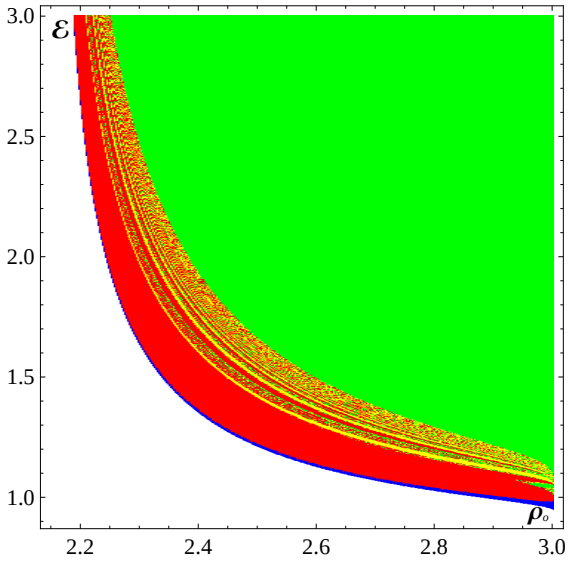

(**b**)

Figure 2.5: Basins of attraction for a charged particle kicked from the ISCO of the given ρ_o (horizontal axis) to different energies (vertical axis). The red zones correspond to capture, the green zones correspond to escape to $z \to +\infty$, and the yellow zones correspond to escape to $z \to -\infty$. (a) is for $\ell > 0$ and (b) is for $\ell < 0$. The step size for both ρ and $\mathcal{E}$ is 2.5×10^{-3}.

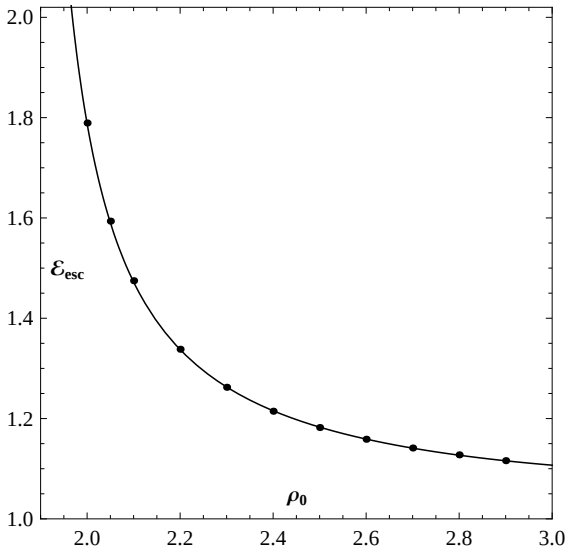

(**a**)

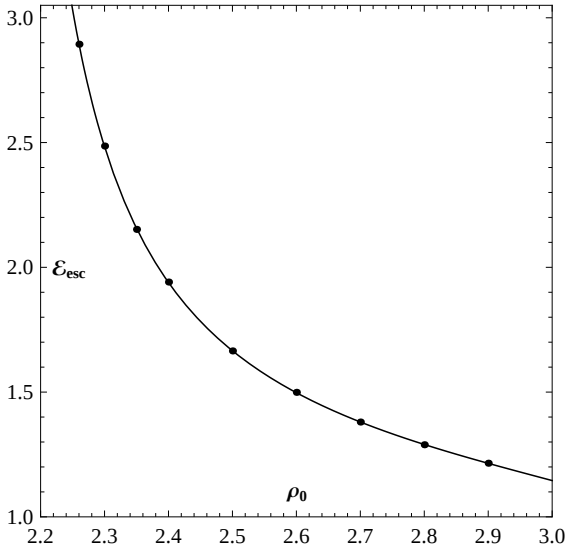

(**b**)

Figure 2.6: Critical escape energy for (a) $\ell > 0$ and (b) $\ell < 0$. The curves are given by the empirical expression (2.44) for (a) and by (2.45) for (b).

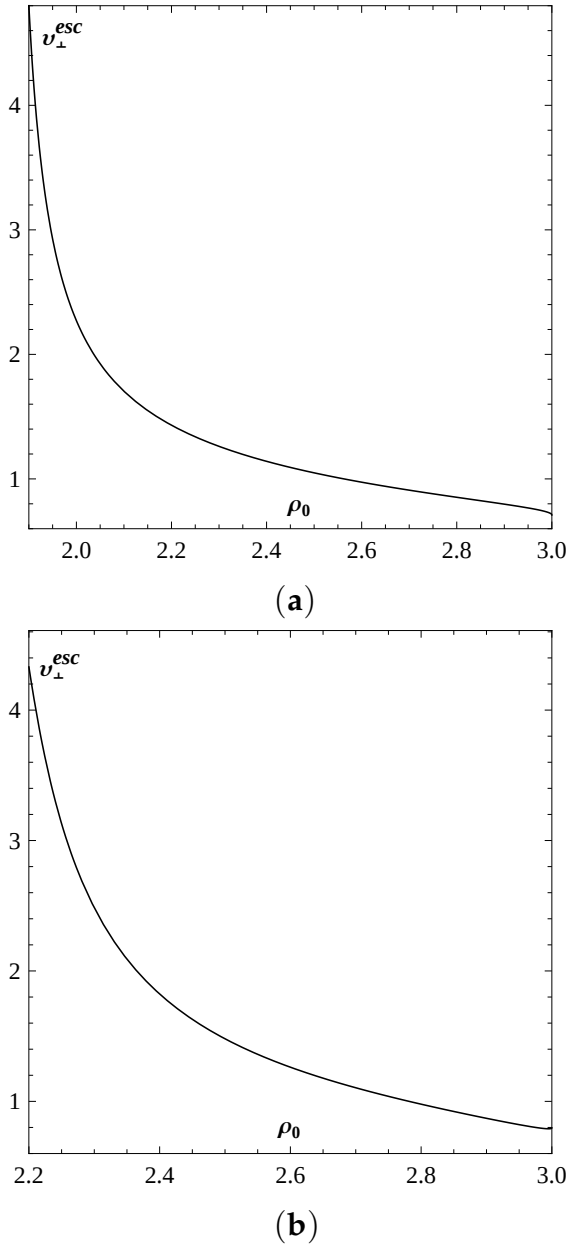

Figure 2.7: Critical escape velocity for (a) $\ell > 0$ and (b) $\ell < 0$.

2.7.3 Near-Critical Behavior

For a given ρ_o and energies close to but less than the critical one, the final state of the particle cannot be strictly predicted. The corresponding near-critical domain contains the final states of all three different types. To illustrate this more clearly let us consider a small strip in these domains. Magnifications of the strips are shown in Fig. 2.8. The horizontal axis on

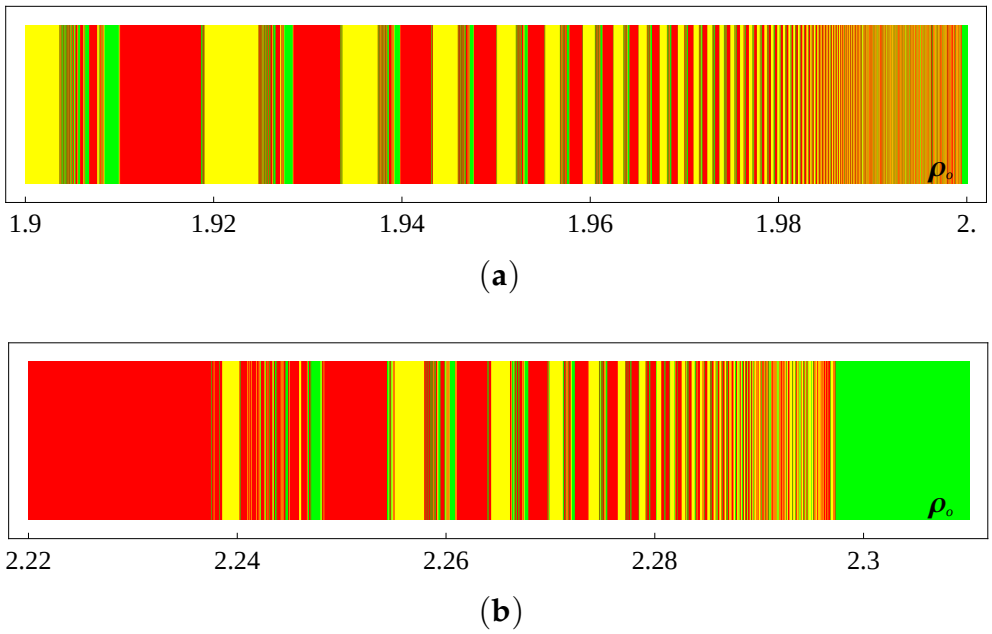

Figure 2.8: Magnified strips from the fractal region in the basins of attraction. (a) A stripe at $\mathcal{E}$ 1.9 for $\ell > 0$. (b) A strip at $\mathcal{E}$ 2.5 for $\ell < 0$.

these plots shows the dimensionless parameter ρ_o of the ISCO, while the vertical axis shows the dimensionless energy $\mathcal{E}$ of the particle after the kick, which is chosen at 1.9 for $\ell > 0$ and at 2.5 for $\ell < 0$. These magnified plots demonstrate the linear structure of different regions corresponding to capture and both types of the escape (corresponding to $n = \pm 1$). Similar magnified strips can be constructed for different values of the magnification factor. The remarkable fact is that each of these plots has a similar

structure, which does not depend on the value of the magnification. In other words, the near-critical diffuse domain has a fractal structure. This fractal structure is a very complicated Cantor-set-like structure, such that a magnification of any portion of the fractal region reveals a similar pattern of the escape and capture regions on a smaller scale, and it continues *ad infinitum*. In the fractal regions the crossing number c corresponding to either escape or capture can take different values and generally increases with the increasing repetition of the patterns.

2.7.4 Fractal Dimension of the Near-Critical Domains

To get a qualitative measure of the complexity of the fractal regions we calculate the box-counting fractal dimension D_f,

$$D_f \equiv \lim_{\epsilon \to 0} \frac{\ln N(\epsilon)}{\ln \frac{1}{\epsilon}}, \quad 1 \leq D_f < 2, \tag{2.46}$$

where $N(\epsilon)$ is the number of squares of the side length ϵ needed to cover a basin boundaries. Such squares are counted only if they contain at least two different colors. The box-counting fractal dimension gives us a quantitative measure of the uncertainty in our numerical computations (see, e.g., Ref. [6]).

Figure 2.9 contains plots of $\ln N(\epsilon)$ vs $\ln(1/\epsilon)$ for different values of ϵ for the fractal structures shown in Fig. 2.5. The plots illustrate a linear relation for sufficiently small values of ϵ. The fractal dimensions of the two basins boundaries are

$$D \approx 1.60, \quad \ell > 0, \tag{2.47}$$

$$D \approx 1.85, \quad \ell < 0. \tag{2.48}$$

The fractal dimension is closer to 2 for the $\ell < 0$ case and thus the corresponding near-critical domain has a more complex fractal structure.

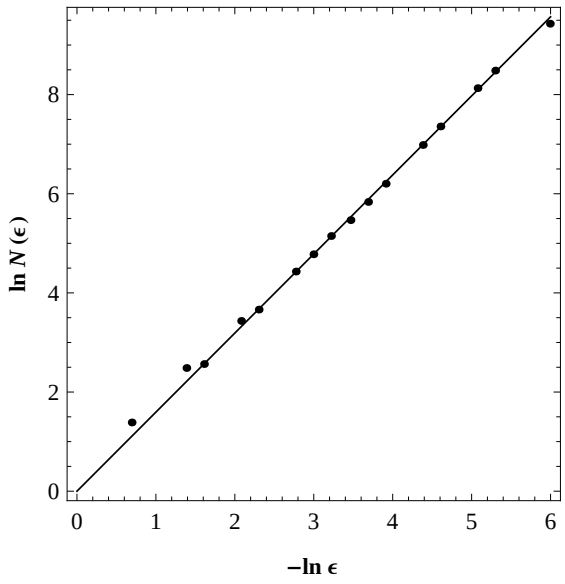

(**a**)

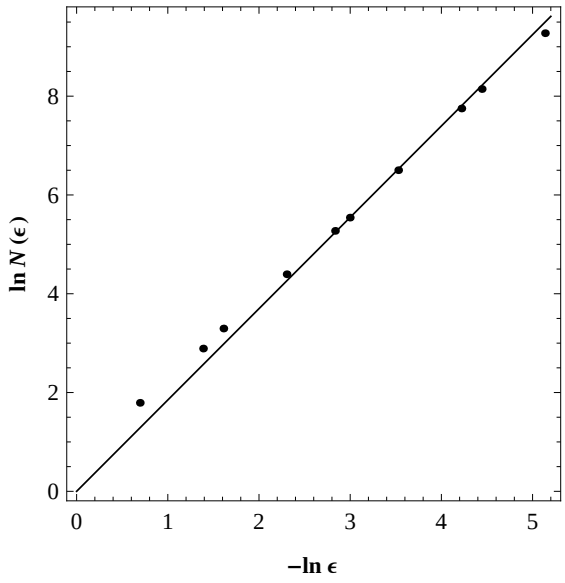

(**b**)

Figure 2.9: The box-counting dimension. Plot (a): $\ln N(\epsilon)$ vs. $\ln(1/\epsilon)$ for $\ell > 0$. Plot (b): $\ln N(\epsilon)$ vs. $\ln(1/\epsilon)$ for $\ell < 0$.

2.7.5 Additional Details of the Basins of Attraction Structure.

We have described the main features of the structure of the domains in the basins of attraction. However, these plots contain additional structure, which we briefly describe now. First of all, let us mention that for $\ell > 0$ and the values of ρ_o in the vicinity of ≈ 1.5 and $\mathcal{E} \gtrsim 1.2$ there is an escape lagoon, illustrated by the yellow color. For the initial data corresponding to this lagoon the charged particle also escapes to infinity but in the direction opposite to the initial kick, that is, with $n = -1$. The crossing number in this region is $c = 1$. Besides this, there are also smaller-size yellow regions that correspond to different values of the crossing number. These regions form a well-visible set of the yellow strips located to the right of the lagoon. Similar yellow strips corresponding to the backscattering to $z \to -\infty$ are present for $\ell < 0$.

2.8 Summary

In this chapter the escape of a charged particle from a weakly magnetized Schwarzschild black hole was studied. The particle—initially at a stable (for neutral particles) or marginally stable (for charged particles) circular orbit—is kicked in the direction normal to the orbital plane. Putting aside possible meta-stable orbits, the particle eventually gets captured by the black hole or escapes it to spatial infinity.

The neutral particle case was tackled first. It was found that it is sufficient for the particle to have energy equal to or greater that its rest energy to ensure escape.

The charged particle problem was found to be more involved where the equations of motion are non-integrable in general. The motion demonstrated chaoticness which made it impossible to write analytical conditions for escape. With the help of the basin of attraction plots, it was possible to write empirical formulae for escape energy for a particle initially at an ISCO.

Bibliography

[1] R. M. Wald, Phys. Rev. D **10**, 1680 (1974).

[2] A. N. Aliev and D. V. Gal'tsov, Sov. Phys. Usp. **32**(1), 75 (1989).

[3] A. N. Aliev and N. Özdemir, Mon. Not. Roy. Astron. Soc. **336**, 241 (2002).

[4] N. Silant'ev, Y. Gnedin, S. Buliga, M. Piotrovich and T. Natsvlishvili, arXiv:1203.2763 (2012).

[5] M. Piotrovich, N. Silant'ev, Y. Gnedin, and T. Natsvlishvili, arXiv:1002.4948 (2010).

[6] E. Ott, *Chaos in Dynamical Systems* (Second edition, Cambridge University Press, New York, USA, 2002).

[7] A. V. Frolov and A. L. Larsen, Classical Quantum Gravity **16** 3717 (1999).

Chapter 3

Escape of Charged Particles Moving around a Weakly Magnetized Kerr Black Hole

3.1 Introduction

In this chapter we study charged particles escape from a weakly magnetized rotating black hole. The simpler case of neutral particles is tackled first. The effect of the black hole's rotation on charged particles escape is investigated. We also discuss the effect of rotation on the chaoticness in the dynamics. The chapter is organised as follows: In Sec. 3.2 we analyse the case of neutral particles. We review particles dynamics and circular orbits in Kerr geometry and then give the escape conditions analytically. In Sec. 3.3 we treat the charged particles case. We discuss their circular orbits and study the ISCOs numerically, and then analyze charged particles dynamics and give the escape conditions. We conclude the chapter with a summary of results in Sec. 3.4.

3.2 Escape Velocity of a Neutral Particle

3.2.1 Circular Orbits

The spacetime geometry around a rotating black hole is described by the Kerr metric. In Boyer-Linquist coordinates, the Kerr metric reads [1]

$$ds^2 = -\Sigma\frac{\Delta}{A}dt^2 + \frac{\Sigma}{\Delta}dr^2 + \Sigma d\theta^2 + \frac{A}{\Sigma}\left(d\phi - \frac{2aMr}{A}dt\right)^2 \sin^2\theta, \tag{3.1}$$

where $\Sigma = r^2 + a^2\cos^2\theta$, $\Delta = r^2 - 2Mr + a^2$, $A = (r^2+a^2)^2 - a^2\Delta\sin^2\theta$. M is the black hole's mass and $J = aM$, with $-M \leq a \leq M$, is its spin angular momentum.

The Kerr spacetime admits two commuting Killing vectors

$$\xi^\mu_{(t)} = \delta^\mu_t, \;\; \xi^\mu_{(\phi)} = \delta^\mu_\phi, \tag{3.2}$$

and a Killing tensor

$$K^{\mu\nu} = \Delta k^{(\mu}l^{\nu)} + r^2 g^{\mu\nu}, \tag{3.3}$$

where

$$l^\mu = \frac{1}{\Delta}\left(r^2+a^2, \Delta, 0, a\right), \tag{3.4}$$

$$k^\mu = \frac{1}{\Delta}\left(r^2+a^2, -\Delta, 0, a\right). \tag{3.5}$$

Consider a particle of mass m in Kerr spacetime moving with four-velocity u^μ. The three Killing symmetries are associated with three constants of the particle's motion

$$-\mathcal{E} = p_\mu \xi^\mu_{(t)}/m, \tag{3.6}$$

$$\mathcal{L} = p_\mu \xi^\mu_{(\phi)}/m, \tag{3.7}$$

$$\mathcal{K} + (\mathcal{L} - a\mathcal{E})^2 = u_\mu u_\nu K^{\mu\nu}, \tag{3.8}$$

where $p^\mu = mu^\mu$ is the particle's four-momentum. $\mathcal{E}$ and $\mathcal{L}$ are the specific energy and azimuthal angular momentum, respectively, and $\mathcal{K}$ is the

Carter constant[1]. Using these three constants of motion along with the normalization $u_\mu u_\mu g^{\mu\nu} = -1$ we can reduce the equations of motion to quadratures:

$$\dot{t} = \mathcal{E} + \frac{2Mr[(r^2+a^2)\mathcal{E} - a\mathcal{L}]}{\Delta\Sigma}, \tag{3.9}$$

$$\dot{\phi} = \frac{\mathcal{L}}{\Sigma \sin^2\theta} + \frac{a(2Mr\mathcal{E} - a\mathcal{L})}{\Delta\Sigma}, \tag{3.10}$$

$$\Sigma^2 \dot{r}^2 = [(r^2+a^2)\mathcal{E} - a\mathcal{L}]^2 - \Delta[r^2 + \mathcal{K} + (\mathcal{L} - a\mathcal{E})^2], \tag{3.11}$$

$$\Sigma^2 \dot{\theta}^2 = \mathcal{K} + (\mathcal{L} - a\mathcal{E})^2 - a^2\cos^2\theta - \left(a\mathcal{E}\sin\theta - \frac{\mathcal{L}}{\sin\theta}\right)^2, \tag{3.12}$$

where the overdot denotes the derivative with respect to the proper time. The particle dynamics is invariant under reflection with respect to the equatorial plane or

$$\theta \to \pi - \theta, \qquad \dot{\theta} \to -\dot{\theta}. \tag{3.13}$$

The dynamics is also invariant under the transformations

$$\phi \to -\phi, \quad \dot{\phi} \to -\dot{\phi}, \quad \mathcal{L} \to -\mathcal{L}, \quad a \to -a. \tag{3.14}$$

Let us define $R(r)$ to be the right hand side of Eq. (3.11)

$$R(r) := [(r^2+a^2)\mathcal{E} - a\mathcal{L}]^2 - \Delta[r^2 + \mathcal{K} + (\mathcal{L} - a\mathcal{E})^2]. \tag{3.15}$$

$R(r)$ is positive semidefinite, it vanishes at radial turning points only. There are two dynamically distinct cases for radial motion, depending on whether the black hole's spin and particle's azimuthal angular momentum are aligned ($a\mathcal{L} > 0$) or oppositely aligned ($a\mathcal{L} < 0$). Without loss of generality, in this chapter $\mathcal{L}$ will be kept positive while a can take both signs. We refer to orbits with $a\mathcal{L} > 0$ as *prograde* and orbits with $a\mathcal{L} < 0$ as *retrograde*.

Circular orbits exist where $R(r)$ and its first derivative $R'(r)$ vanish. For

[1]The second term on the LHS of Eq. (3.8) does not appear in the standard definition of Carter constant. We chose our definition for convenience.

equatorial orbits ($\theta = \frac{\pi}{2}, \mathcal{K} = 0$), these two conditions yield

$$[(r^2 + a^2)\mathcal{E} - a\mathcal{L}]^2 - \Delta[r^2 + (\mathcal{L} - a\mathcal{E})^2] = 0, \quad (3.16)$$

$$2r\mathcal{E}[(r^2 + a^2)\mathcal{E} - a\mathcal{L}] - 2r\Delta - 2(r - M)[r^2 + (\mathcal{L} - a\mathcal{E})^2] = 0. \quad (3.17)$$

We will use r_o, $\mathcal{E}_o$ and $\mathcal{L}_o$ to denote circular orbits from here on. Solving for $\mathcal{E}_o$, $\mathcal{L}_o$ one obtains after tedious algebra

$$\mathcal{E}_o = \frac{aM^{1/2} + r_o^{1/2}(r_o - 2M)}{\sqrt{2aM^{1/2}r_o^{3/2} + r_o^2(r_o - 3M)}}, \quad (3.18)$$

$$\mathcal{L}_o = \frac{M^{1/2}(a^2 + r_o^2) - 2aMr_o^{1/2}}{\sqrt{2aM^{1/2}r_o^{3/2} + r_o^2(r_o - 3M)}}. \quad (3.19)$$

The radius of the last circular orbit r_{lc}, is given by

$$r_{lc} = \frac{[M + M^{1/3}(\sqrt{a^2 - M^2} - a)^{2/3}]^2}{M^{1/3}(\sqrt{a^2 - M^2} - a)^{2/3}}. \quad (3.20)$$

Plugging r_{lc} in Eq. (3.18) reveals that $\mathcal{E}_o$ is positive for all circular orbits. A particle is at an ISCO when $R''(r)|_{r=r_o}$ vanishes, or

$$(6r_o^2 + a^2)(\mathcal{E}_o^2 - 1) + 6Mr_o - \mathcal{L}_o^2 = 0. \quad (3.21)$$

Plugging the $\mathcal{E}_o$ and $\mathcal{L}_o$ values above in this condition one obtains

$$r_{ms}(r_{ms} - 6M) + 8a\sqrt{Mr_{ms}} - 3a^2 = 0. \quad (3.22)$$

We used r_{ms} (for *marginally stable*) to denote the ISCOs. The $\mathcal{E}_o$ and $\mathcal{L}_o$ expressions reduce for an ISCO to

$$\mathcal{L}_{ms}^2 = \frac{2}{3}\frac{M}{r_{ms}}(3r_{ms}^2 - a^2), \quad \mathcal{E}_{ms}^2 = 1 - \frac{2}{3}\frac{M}{r_{ms}}. \quad (3.23)$$

Fig. 3.1 shows how r_{ms} changes with a. For $a = M$, $a = -M$ one gets $r_{ms} = M$, $r_{ms} = 9M$, respectively. r_{ms} becomes $6M$ when $a = 0$ as expected.

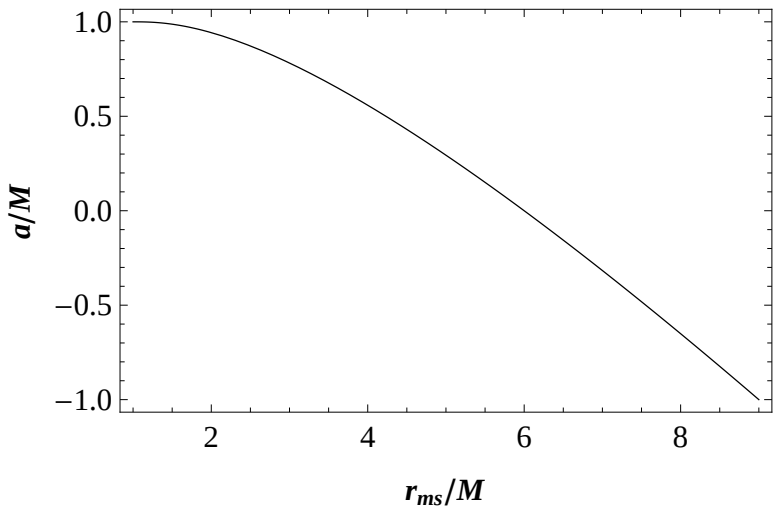

Figure 3.1: The radius of the last stable circular orbit r_{ms} vs. the black hole's rotation parameter a.

3.2.2 Conditions for Escape from a Circular Orbit

Three-Dimensional Motion

Consider a particle at a stable circular orbit r_o that has the four-velocity $u_\mu = (-\mathcal{E}_o, 0, 0, \mathcal{L}_o)$. As we mentioned above the particle is kicked in such a way that it only acquires velocity parallel (or antiparallel) to the axis of the black hole rotation. The kick changes the particle's four-velocity to $u_\mu = (-\mathcal{E}, 0, r_o^3\dot{\theta}_k, \mathcal{L}_o)$, where $\dot{\theta}_k = -v_\perp / r_o$. We can express the dependence of $\mathcal{E}$ and $\mathcal{K}$ on $\dot{\theta}_k$ using Eqs. (3.11) and (3.12). The expressions are

$$\begin{aligned} \mathcal{E} &= \frac{1}{r_o^3 + a^2(r_o + 2M)}\Big[2a\mathcal{L}_o M + \Delta^{1/2} \\ &\quad \sqrt{a^2(r + 2M)(r_o^3\dot{\theta}_k^2 + r_o) + r_o^2(r_o^4\dot{\theta}_k^2 + r_o^2 + \mathcal{L}_o^2)}\Big] \qquad (3.24) \\ \mathcal{K} &= r_o^4\dot{\theta}_k^2. \qquad (3.25) \end{aligned}$$

The positive root for the energy was selected to have the four-velocity vector future-directed. To study the particle's behaviour after the kick it

is more appropriate to recast Eq. (3.11) as

$$\Sigma^2 \dot{r}^2 = r[r^3 + a^2(r+2M)](\mathcal{E} - V_+)(\mathcal{E} - V_-), \tag{3.26}$$

where

$$\begin{aligned} V_\pm(r) &= \frac{1}{r^3 + a^2(r+2M)}\Big[2a\mathcal{L}M \pm \Delta^{1/2} \\ &\quad \sqrt{a^2(r+2M)(\mathcal{K}/r + r) + r^2(\mathcal{K} + r^2 + \mathcal{L}^2)}\Big], \end{aligned} \tag{3.27}$$

where again $V_+(r)$ will be considered for future-directed four-velocity vector. In order to determine the escape conditions we need to inspect the effective potential $V_+(r)$ to figure out how a particle will move after getting kicked.

Escape Conditions

The effective potential $V_+(r)$ becomes unity far away from the black hole. Trivially, the particle must be energetically unbound ($\mathcal{E} \geq 1$) to be able to escape. The $\dot{\theta}_k$ value at which the particle becomes energetically unbound is designated by $\dot{\theta}_{\mathcal{E}=1}$. We use Eqs. (3.25) and (3.27) to express it as

$$|\dot{\theta}_{\mathcal{E}=1}| = \left[\frac{2M[(a - \mathcal{L}_o)^2 + r_o^2] - \mathcal{L}_o^2 r_o}{\Delta r_o^3}\right]^{1/2}. \tag{3.28}$$

We will assume that the trivial condition $|\dot{\theta}_k| \geq |\dot{\theta}_{\mathcal{E}=1}|$ is always satisfied.

Unfortunately, energetic freedom is not sufficient for the particle to escape when $a > 0$. Depending on the black hole's parameters, particle's initial conditions and the kick strength $|\dot{\theta}_k|$, the particle may accelerate both away or toward the black hole. The particle will experience only one radial turning point and hence the sign of the radial acceleration $\ddot{r}$ just after the kick determines whether it escapes or gets captured. An example is shown in Fig. 3.2.

Careful inspection of $V_+(r)$ reveals that there are *three* distinct regions in which the kicked particle accelerates in a specific way. The three re-

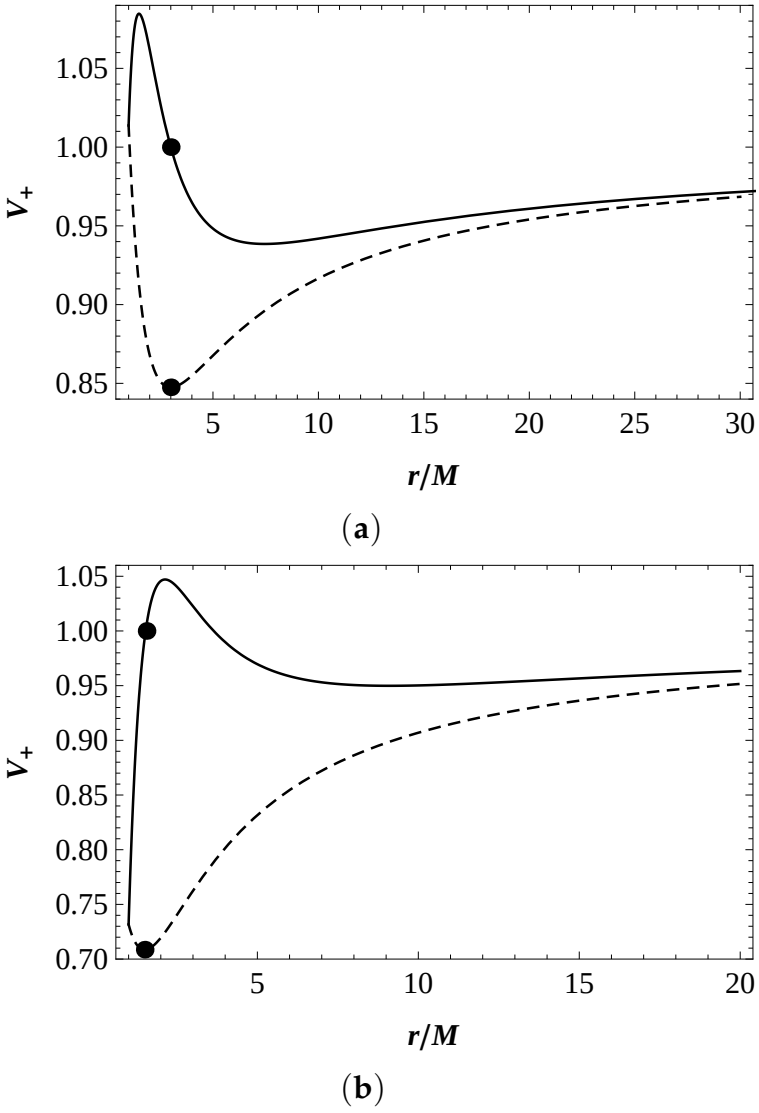

Figure 3.2: $V_+(r)$ for a particle before (dashed line) and after (solid line) getting kicked to energy $\mathcal{E} = 1$. (a) The particle accelerates away from the black hole after getting kicked from a circular orbit at $r_o = 3M$. (b) The particle accelerates toward the black hole after getting kicked from a circular orbit at $r_0 = 3/2M$. In both cases $a = M$.

gions are as follows:

- **Escape region**: In this region $\ddot{r} > 0$ for any $\dot{\theta}_k$. The acceleration is proportional to the kicking energy. The escape region is given by $r > r_{esc}$, where r_{esc} is determined by the equation

$$(r_{esc} - 3M)r_{esc}^2 + a^2(r_{esc} + M) = 0. \tag{3.29}$$

  The particle oscillates around the initial orbit if $|\dot{\theta}_k| \ll |\dot{\theta}_{\mathcal{E}=1}|$. The ISCO is located in this region when $a \lesssim 0.853M$.

- **Capture region**: In this region $\ddot{r} < 0$ for any $\dot{\theta}_k$. The stronger is the kick the faster the capture is. This region lies in the interval $r_H \leq r < r_{cap}$, where r_H is the black hole's event horizon and r_{cap} is given by the equation

$$M^{1/2}(ar_{cap}^2 + a^3) + (r_{cap} - 3M)r_{cap}^{5/2} + a^2(r_{cap} - M)r_{cap}^{1/2} = 0. \tag{3.30}$$

  The particle will be always captured unless if the kick is tiny. It will just oscillate around the initial orbit in that case. The orbit at $r_o = M$ (when $a = M$) is an exception. That is because Eq. (3.24) reduces to $\mathcal{E} = 1/\sqrt{3}$, which means that the particle becomes irresponsive to the kick. The ISCO is located in the capture region for $M \geq a \gtrsim 0.952M$.

- **The critical escape region**: The particle acceleration is more involved in this region because its direction depends on $|\dot{\theta}_k|$ value. $\ddot{r} > 0$ if $|\dot{\theta}_k|$ is below some critical value $|\dot{\theta}_c|$. For $|\dot{\theta}_k| > |\dot{\theta}_c|$, the acceleration becomes inwards. For orbits with $|\dot{\theta}_{\mathcal{E}=1}| > |\dot{\theta}_c|$, the particle can never escape. The critical escape region lies between the escape and capture regions. $\dot{\theta}_c$ is determined by

$$\partial_r V_+(r, \dot{\theta}_c) = 0; \quad r_{cap} < r < r_{esc}. \tag{3.31}$$

  In Fig. 3.3 we plot $|\dot{\theta}_c|$ and $|\dot{\theta}_{\mathcal{E}=1}|$ vs. r_o for $a = 0.95M$. We see that $|\dot{\theta}_c|$ vanishes at $r_{cap} \approx 1.92M$ and approaches infinity as r_o approaches

$r_{esc} \approx 2.49M$. Figure 3.4 shows how the initial orbit radius r_o at which $|\dot{\theta}_c| = |\dot{\theta}_{\mathcal{E}=1}|$ changes with a. It is always greater than r_{cap}.

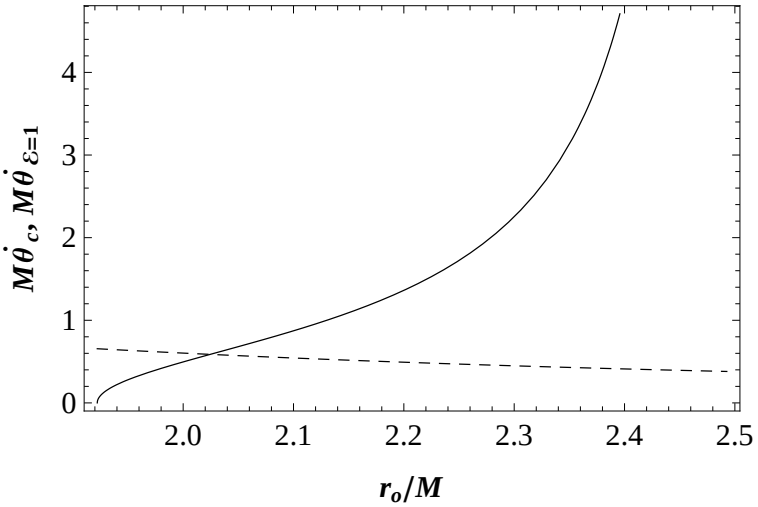

Figure 3.3: $|\dot{\theta}_c|$ (solid) and $|\dot{\theta}_{\mathcal{E}=1}|$ (dashed) vs. r_o for $a = 0.95M$. $|\dot{\theta}_c|$ vanishes at r_{cap} and approached infinity as r_o approaches r_{esc}.

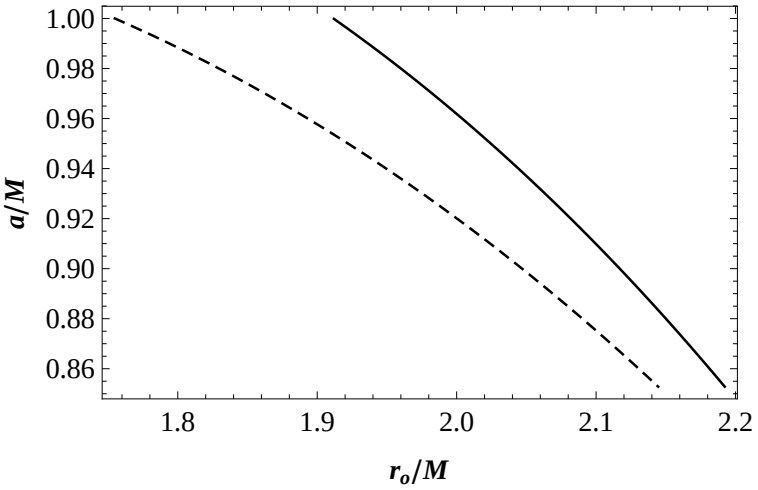

Figure 3.4: The radius of the initial orbit r_o at which $|\dot{\theta}_c| = |\dot{\theta}_{\mathcal{E}=1}|$ (solid) as a function of a. The dashed curve is r_{cap}.

Figure 3.5 shows the three regions along with the ISCO and how they change with a. Incorporating all of the above analyses, a particle in a circular orbit around a Kerr black hole kicked in the direction normal to the orbit can escape in the following two cases:

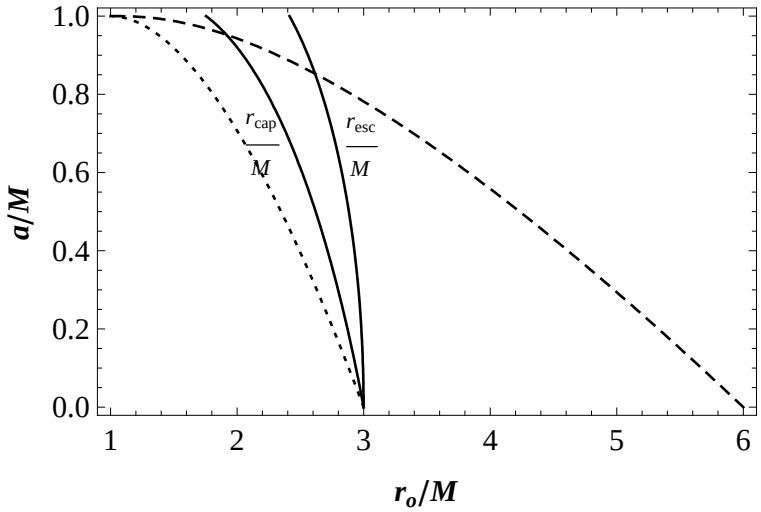

Figure 3.5: The dependence of r_{esc}, r_{cap} and r_{ms} (dashed) on a. The escape region is to the right of r_{esc}, the capture region is to the left of r_{cap}, while the critical escape region is the one in between. The dotted line is r_{lc}.

1. Its initial orbit is in the escape region, $r_o \geq r_{esc}$.
2. Its initial orbit is in the critical escape region, $r_{cap} < r_o < r_{esc}$, where it is possible to have $|\dot{\theta}_{\mathcal{E}=1}| \leq |\dot{\theta}_o| < |\dot{\theta}_c|$.

3.3 Escape Velocity of a Charged Particle

3.3.1 Circular Orbits

The particle's energy and azimuthal angular momentum are still constants of motion since the electromagnetic potential Eq. (2.19) is invariant with respect to the temporal and azimuthal Killing isometries

$$\mathcal{L}_{\xi_{(t)}} A^\mu = \mathcal{L}_{\xi_{(\phi)}} A^\mu = 0. \tag{3.32}$$

The specific energy $\mathcal{E}$ and azimuthal angular momentum $\mathcal{L}$ are

$$-\mathcal{E} = P_\mu \xi^\mu_{(t)}/m = \left(\frac{2Mr}{\Sigma} - 1\right)\dot{t} - \frac{2aMr}{\Sigma}(b+\dot{\phi})\sin^2\theta, \quad (3.33)$$

$$\mathcal{L} = P_\mu \xi^\mu_{(\phi)}/m = \left[-\frac{2aMr}{\Sigma}\dot{t} + \frac{A}{\Sigma}(b+\dot{\phi})\right]\sin^2\theta, \quad (3.34)$$

where $b = qB/2m$. The introduction of A^μ breaks down the Carter integral of motion. It can be checked by direct differentiation with respect to the proper time that $\dot{\mathcal{K}} \neq 0$. Using the normalization condition $u^\mu u_\mu = -1$ along with Eqs. (3.33) and (3.34) one can write

$$\begin{aligned}\Sigma^2\left(\dot{r}^2 + \Delta\dot{\theta}^2\right) &= A\mathcal{E}^2 - 4aM\mathcal{E}\mathcal{L}r - \Delta\Sigma(1-2b\mathcal{L}) \\ &+ \frac{\mathcal{L}^2(2Mr-\Sigma)}{\sin^2\theta} - b^2 A\Delta\sin^2\theta. \end{aligned} \quad (3.35)$$

This equation simplifies in the equatorial plane to

$$\begin{aligned} r^3\dot{r}^2 &= (\mathcal{E}^2 - b^2\Delta)[r(r^2+a^2) + 2Ma^2] - 4aM\mathcal{E}\mathcal{L} \\ &- r\Delta(1-2b\mathcal{L}) - \mathcal{L}^2(r-2M). \end{aligned} \quad (3.36)$$

There are *four* dynamically distinct cases of equatorial motion. They are determined by the four combinations of the signs of $b\mathcal{L}$ and $a\mathcal{L}$. As mentioned above, we fix $\mathcal{L}$ to be positive. We just alter the signs of a and b to consider the four cases. We refer to the $b > 0$ ($b < 0$) case as anti-Larmor (Larmor) motion. The radial acceleration of the particle $f^r = \frac{q}{m}F^{r\nu}u_\nu$ is positive (negative) in the anti-Larmor (Larmor) case. Let define $U(r)$ to be the right hand side of Eq. (3.36)

$$\begin{aligned} U(r): &= (\mathcal{E}^2 - b^2\Delta)[r(r^2+a^2) + 2Ma^2] - 4aM\mathcal{E}\mathcal{L} \\ &- r\Delta(1-2b\mathcal{L}) - \mathcal{L}^2(r-2M). \end{aligned} \quad (3.37)$$

Then using the circular orbit conditions $U(r) = 0$ and $U'(r) = 0$ one ob-

tains

$$(\mathcal{E}^2 - b^2\Delta)[r(r^2+a^2)+2Ma^2] - 4aM\mathcal{E}\mathcal{L} - r\Delta(1-2b\mathcal{L} - \mathcal{L}^2(r-2M) = 0, \quad (3.38)$$

$$2b^2(r-M)[r(r^2+a^2)+2Ma^2] + (1-2b\mathcal{L})[2r(r-M)+\Delta] - (\mathcal{E}^2 - b^2\Delta)(3r^2+a^2) + \mathcal{L}^2 = 0. \quad (3.39)$$

The extra condition for ISCOs $U''(r) = 0$ gives

$$(2b\mathcal{L}-1)(3r-2M) + 3\mathcal{E}^2 r - 2b^2 r[r(5r-6M)+3a^2] = 0. \quad (3.40)$$

It seems possible to solve Eqs. (3.38) and (3.39) and obtain analytic expressions for $\mathcal{E}_o$ and $\mathcal{L}_o$, however, the resulting expressions are extremely complicated. We solve these equations numerically instead. We also require that $\dot{t} > 0$ to exclude past-directed solutions. Using Eqs. (3.33) and (3.34), an expression for $\dot{t}$ in the equatorial plane can be written as

$$r\Delta\dot{t} = [r^3 + a^2(r+2M)]\mathcal{E} - 2a\mathcal{L}M. \quad (3.41)$$

It is interesting to see how the ISCO depends on a for selected values of the magnetic parameter b. Knowing the dependence of the ISCO on a is essential for measuring the spins of astrophysical black holes [2]. The a–r_{ms} curves are shown for selected b values in Fig. 3.6. When $b = 0$ Fig. 3.1 is reproduced. In both Larmor and anti-Larmor motions r_{ms} gets closer to the black hole as $|b|$ increases. It converges to an asymptotic value as $|b|$ becomes large. The shift in r_{ms} is more evident in the anti-Larmor motion case. The value of r_{ms} is different from the asymptotic value by less than 0.1% when $5.8 \times 10^3 < b < -0.82M^{-1}$. For retrograde motion r_{ms} is always outside the static limit. Figures 3.7 and 3.8 show $\mathcal{L}_{ms}$ and $\mathcal{E}_{ms}$ corresponding to the ISCOs shown in Fig. 3.6. It is interesting that negative energy stable circular orbits can exist in the retrograde anti–Larmor motion. The possibility for the existence of negative extra-ergospheric energy states was pointed out in [3] and further explored in [4]. The energy-emission processes related to it were discussed in [5, 6].

$\mathcal{E}_{ms}$ becomes zero at $a = -M$ when $b = b_c$, where $b_c = xM^{-1}$ and x is the positive real root of

$$45056x^{12} - 52224x^{10} + 3072x^8 - 3776x^6 + 4656x^4 - 1320x^2 = 25. \quad (3.42)$$

Approximately $x = 1.05344$. As b increases further $\mathcal{E}_{ms}$ becomes negative for $a \geq -M$. Asymptotically, $\mathcal{E}_{ms}$ becomes negative for all retrograde anti-Larmor orbits and approaches a minimum of $2(1 - \sqrt{2})Mb$ at $a = -M$ where $r_{ms} = (1 + \sqrt{2})M$. This immense binding energy is intriguing. A charged particle of mass m_q and $b \gg M^{-1}$ ending up in this 'superbound' state can give off energy

$$E = m_q \mathcal{E}_{ms} = (\sqrt{2} - 1)qBM. \quad (3.43)$$

For typical stellar mass and supermassive black holes of masses M_{St} and M_{Su}, respectively, this amounts to

$$E = 1.832 \times 10^6 (\frac{M_{St}}{M_\odot}) GeV, \quad (3.44)$$

$$E = 1.832 \times 10^2 (\frac{M_{Su}}{M_\odot}) GeV, \quad (3.45)$$

where $M_\odot$ is the solar mass.

It should be noted that there is only one r_{ms} solution after past-directed orbits are excluded. The equation for r_{ms} given in [7] yields future-directed solutions only when $b < b_c$.

3.3.2 Three-Dimensional Motion and Conditions for Escape from a Circular Orbit

It does not seem possible to determine the escape conditions analytically due to the lack of a fourth constant of motion. The r and θ components of the dynamical equation[2] (2.20) were solved using the built-in *MATHE-*

[2]See the appendix at the end of this chapter Sec. 3.5 for the explicit forms of these components.

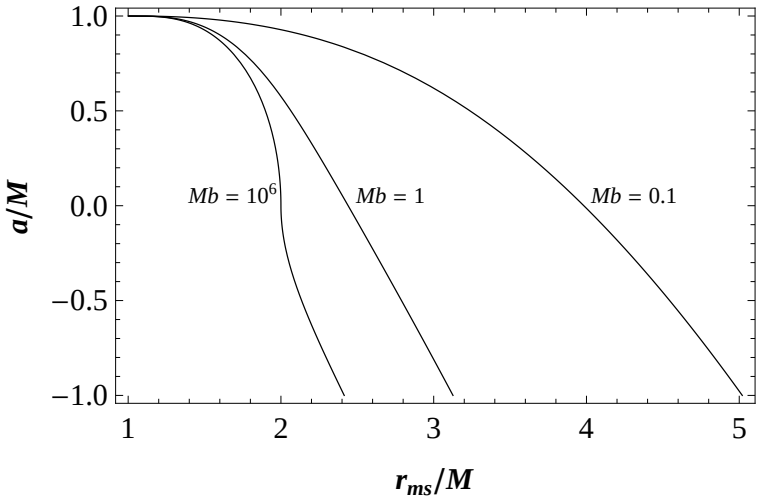

(**a**)

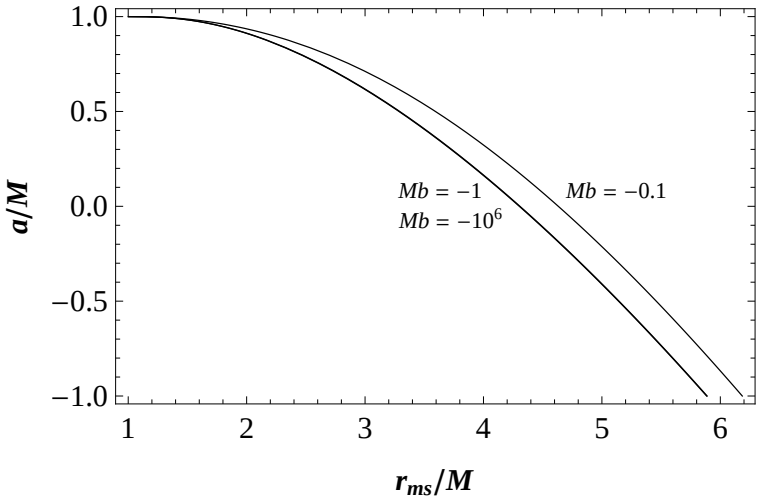

(**b**)

Figure 3.6: The ISCO's radius r_{ms} dependence on a for different values of the magnetic parameter b for (a) anti–Larmor and (b) Larmor motion.

MATICA 7.0 function NDSOLVE. We used the constant of motion $\mathcal{E}$ as a gauge of error in the numerical solver as before.

The numerical integration reveals that the escape and capture regions are more involved than those in the neutral particle case. In Fig. 3.9 the trajectories of a charged particle kicked to three different energies $\mathcal{E} = 1.0890$, $\mathcal{E} = 1.0893$ and $\mathcal{E} = 1.0900$ are shown. $\mathcal{E}$ is related to $\dot{\theta}_k$ by Eq. (3.35). As in the Schwarzschild black hole case, the particle in each case ends up following a completely different trajectory despite that the difference in energies is tiny. This extreme sensitivity to initial conditions is an indicator of chaos. To obtain a comprehensive view of the problem we will need to identify which initial conditions lead to escape and which lead to capture. As we did in Ch. 2, we use the basin of attraction for this purpose.

Let us see how the basin of attraction looks like for a neutral particle first. We use the same color notation adopted in Ch. 2. Fig. 3.10 shows the basin of attraction for a neutral particle generated numerically with initial values of $r_o \in (r_{lc}, r_{lc} + 6M)$ plotted horizontally and initial values of $\mathcal{E} \in (1.0, 2.0)$ plotted vertically. The resolution of the plot is 600×600. The state of the particle is considered an escape if it reaches $200M$. This escape criterion is very efficient even when the particle is charged and hence was adopted in this chapter. The maximum integration time is $10^5 M$. We tackled the $a = 0.999M$ case, where $r_{lc} = 1.052M$, because the structure of the basin of attraction in this case is the richest. The basin boundaries are regular as they should be for a regular system. The structure of the attractors is in accord with that described analytically in Sec. 3.2.2. The red color approaches r_{esc} as $\mathcal{E}$ becomes very large. The particle is backscattered near r_{esc} and at low energies, where it barely makes it to escape.

Now we return to charged particles. Figure. 3.11 shows the basins of attraction for anti-Larmor motion ($b = 0.1M^{-1}$) with initial values of $r_o \in (r_{ms}, r_{ms} + 6M)$ plotted horizontally and initial values of $\mathcal{E} \in (1.0, 2.0)$ plotted vertically. Figure. 3.12 shows the Larmor motion ($b = -0.1M^{-1}$) basins of attraction but with initial values of $\mathcal{E} \in (1.0, 3.0)$ since $\mathcal{E}_0$ is usually considerably larger than 1. The value of $|b|$ considered here may be

small compared to typical astrophysical values. Nonetheless, we find this value appropriate to demonstrate the various aspects of the problem. The resolution of the plots in these figures is 800×800. The spin parameter a was taken at selected values between -1 and 1. The similarity between Fig. 3.10 and 3.11 (f) is striking. The main effect of the magnetic field is to distort the basin boundaries from regular lines to fractals.

Let is discuss the general structures of the basins of attraction and formulate the escape conditions. The main parts in the basins of attraction can be identified as follows:

- **Escape region**: In this region particles escape directly in the direction of the kick. This region is the upper right large green area in the figures. It gets reduced from left as a increases. We use the boundary of this region to define the effective escape energy $\mathcal{E}_{esc}$, which can be linked to a corresponding $\dot{\theta}_{esc}$ through Eq. (3.35). This effective escape energy curve can be fitted with a tiny relative error to a function of the form

$$\mathcal{E}_{esc} = 1 + \frac{a + br_o + cr_o^2}{d + er_o + fr_o^2}. \tag{3.46}$$

  where $a, b, ...$ and f are fitting parameters.

- **Capture region**: This is the red nearly rectangular area in the left side of the plots when $a = 0.999M$. The particle is always swallowed by the black hole in this region for any energy. It is the proximity of r_o from the horizon that makes particles always accelerate inward no matter how energetic the kick is. Therefore this region shows up only when a is close to M. Increasing b for anti-Larmor motion (see Fig. 3.6) would also leads to the emergence of this region because r_{ms} would become closer to the horizon.

- **Fractal region**: The escape region is most of the time bounded by a region of extremely fine threads that demonstrate a repetitive pattern of red, green and yellow colors. These threads get finer as they

get closer from the escape region. We refer to this region as the fractal region. The particle in it may cross the equatorial plane several times. The fractal structure is persistent at any magnification level. The red color ceases to exist near the end of the horizontal tail of the fractal. This effect becomes more noticeable as a increases until the red color completely disappears from the lower half of the fractal structure when $a = 0.999M$.

- **Stability region**: It is represented by the blue strip in the Larmor motion plots. We expected that the left boundary of this region becomes smooth if the numerical integrator is run for longer time. However, increasing the integration time will increase the computation time immensely without modifying significantly the quantity we want to measure, namely D_f (see below).

- **Backscattering region**: It is the yellow isle located between the capture region and the upper branch of the fractal region. In the backscattering region the particle escapes in the direction opposite to the kick. Like the capture region, the backscattering region appears when r_o is close from the horizon.

3.3.3 Rotation and Chaoticness

It is interesting to see how the black hole's spin a affects the chaoticness in the dynamics. We use the fractal dimension D_f of the basin boundary as a measure of chaoticness. It should be mentioned that D_f cannot be used to make a general conclusion since the basins of attraction are produced for specific ranges of initial conditions. Moreover, r_{ms} depends on a and one should be consistent when choosing the ranges of initial conditions for different values of a. We therefore prefer to take the ranges of initial conditions identical to those of the basins of attraction in Figs. 3.11 and 3.12, in particular $r_o \in (r_{ms}, r_{ms} + 6M)$. Although $\mathcal{E}_o$ in the Larmor motion depends strongly on a as well we choose to keep the range of $\mathcal{E}$ as before for brevity. The dependence of D_f on a for the specified ranges of

initial conditions is shown in Fig. 3.13 for (a) anti-Larmor motion and (b) Larmor motion.
For Larmor retrograde motion D_f is nearly constant while it is linearly increasing (within error) for the remaining cases. It is not surprising that D_f increases with a since the gravitational field gets stronger as r_{ms} gets closer to the horizon. As mentioned above, the D_f–a relation depends on the set of initial conditions. For example, D_f becomes inversely proportional to a if $r_o \in (4M, 10M)$ is chosen instead!

3.4 Summary

In this chapter the escape of charged particles orbiting a weakly magnetized Kerr black hole was investigated. The magnetic field is parallel or anti-parallel to the black hole's spin. The particle is kicked from a stable circular orbit in the direction perpendicular to the orbit's plane. We studied the case of neutral particles first and gave the escape conditions analytically. It was found that there are three regions in which the particle behaves in a specific way after the kick. If the particle's orbit is far enough from the black hole it accelerates away and escapes if it has sufficient energy. If it is too close it accelerates inwardly and gets captured unless if the kick energy is tiny. Between the two regions the particle accelerates away if the kick velocity is below some critical velocity. The particle can escape if it can be made energetically unbound before reaching the critical kick velocity.

We have written the equations determining the stable and marginally stable circular orbits and studied the latter numerically. A result of special interest is that extra-ergospheric stable circular orbits with negative energies can exist. It was shown that a particle can give off energy several orders of magnitude greater than its rest energy if it ends up in a 'superbound' orbit. The energy released is independent of the falling particle mass when $b \gg M^{-1}$.

The case of charged particles escape has two extra complications: (1) The magnetic field shifts the ISCO inward, and more importantly (2) the

dynamics becomes chaotic. By inspecting the basins of attraction for neutral and charged particles we find that the main effect of the magnetic field is to make the basin boundaries fractals instead of simple curves. We identified several regions of interest in the basins of attraction and gave an empirical criterion for charged particles guaranteed escape.

It seems that the particle escape becomes more difficult as the black hole's rotation parameter increases because the ISCO becomes closer to the horizon. However, if a whole accretion disk is considered then the dependence is more involved. No general conclusion about the relation between chaoticness and black hole's rotation was found, mainly because our measure of chaoticness, the fractal dimension, is strongly dependant on the ranges of initial conditions selected. In spite of that, it seems true that the dynamics gets more chaotic when the gravitational field gets stronger.

Increasing the values of $|b|$ would modify the dynamics, especially in the anti-Larmor motion since r_{ms} would be significantly affected. Nevertheless, we don't expect that to show new aspects of the problem.

3.5 Appendix

In this appendix we write the r and θ components of the dynamical equation (2.20) in Kerr background explicitly. They read

$$\begin{aligned}
\ddot{r} &= \frac{M\Delta(2r^2-\Sigma)}{\Sigma^3}\left(2a\sin^2\theta\,\dot{t}\dot{\phi}-\dot{t}^2\right)+\frac{r\Delta}{\Sigma}\dot{\theta}^2-\left(\frac{r}{\Sigma}-\frac{\Delta_{,r}}{2\Delta}\right)\dot{r}^2 \\
&- \frac{\Sigma_{,\theta}}{\Sigma}\dot{r}\dot{\theta}-\frac{\Delta(2rA-\Sigma A_{,r})\sin^2\theta}{2\Sigma^3}\dot{\phi}^2 \\
&+ qB\left[\frac{aM\Delta(2r^2-\Sigma)\sin^2\theta}{\Sigma^3}\dot{t}-\frac{\Delta(2rA-\Sigma A_{,r})\sin^2\theta}{2\Sigma^3}\dot{\phi}\right], \qquad (3.47) \\
\ddot{\theta} &= -\frac{2r}{\Sigma}\dot{r}\dot{\theta}-\frac{Mr\Sigma_{,\theta}}{\Sigma^3}\dot{t}^2-\frac{\Sigma_{,\theta}}{2\Sigma}\dot{\theta}^2+\frac{\Sigma_{,\theta}}{2\Delta\Sigma}\dot{r}^2-\frac{2aMr(2\Sigma\cos\theta-\Sigma_{,\theta}\sin\theta)\sin\theta}{\Sigma^3}\dot{t}\dot{\phi} \\
&- \frac{[A(\Sigma_{,\theta}\sin\theta-2\Sigma\cos\theta)-\Sigma A_{,\theta}\sin\theta]\sin\theta}{2\Sigma^3}\dot{\phi}^2 \\
&- qB\left\{\frac{aMr(2\Sigma\cos\theta-\Sigma_{,\theta}\sin\theta)\sin\theta}{\Sigma^3}\dot{t}\right. \\
&+ \left.\frac{[A(\Sigma_{,\theta}\sin\theta-2\Sigma\cos\theta)-\Sigma A_{,\theta}\sin\theta]\sin\theta}{2\Sigma^3}\dot{\phi}\right\}, \qquad (3.48)
\end{aligned}$$

We then eliminate $\dot{t}$ and $\dot{\phi}$ using Eqs. (3.33) and (3.34).

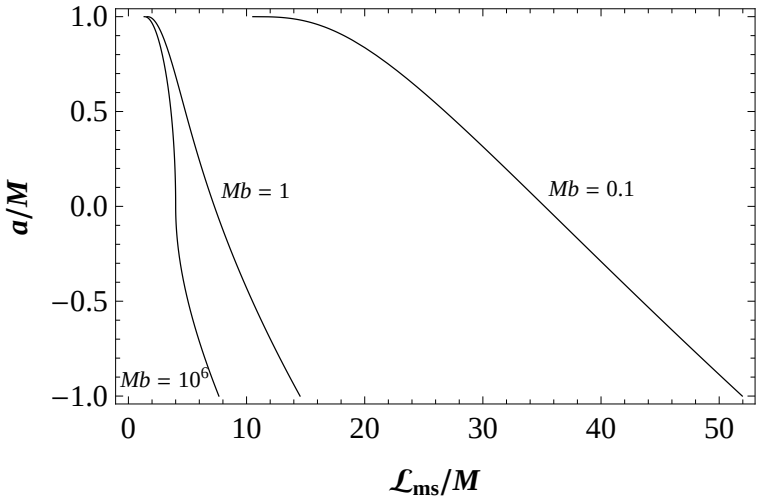

(**a**)

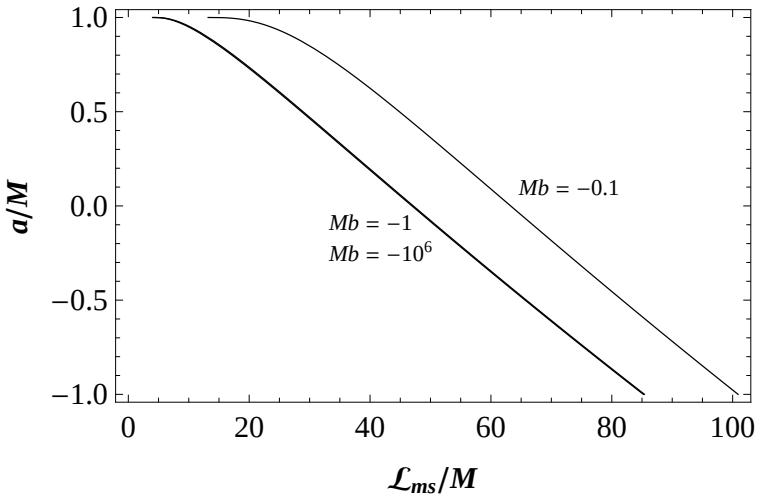

(**b**)

Figure 3.7: The ISCO's azimuthal angular momentum $\mathcal{L}_{ms}$ dependence on a for different values of the magnetic parameter b for (a) anti–Larmor and (b) Larmor motion.

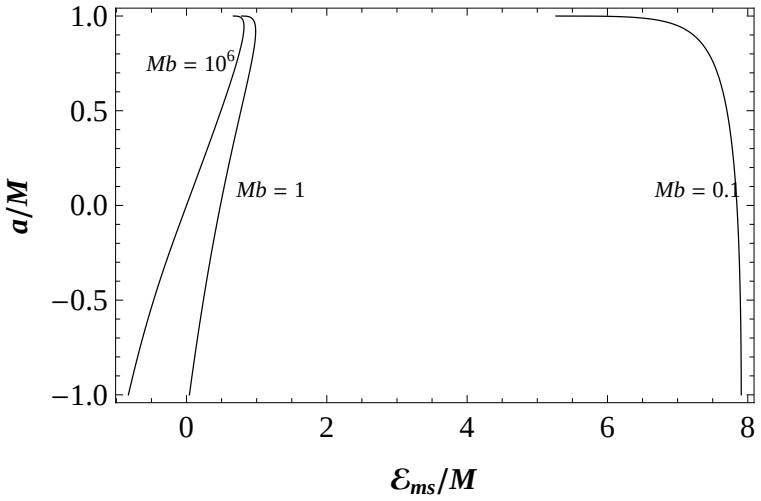

(**a**)

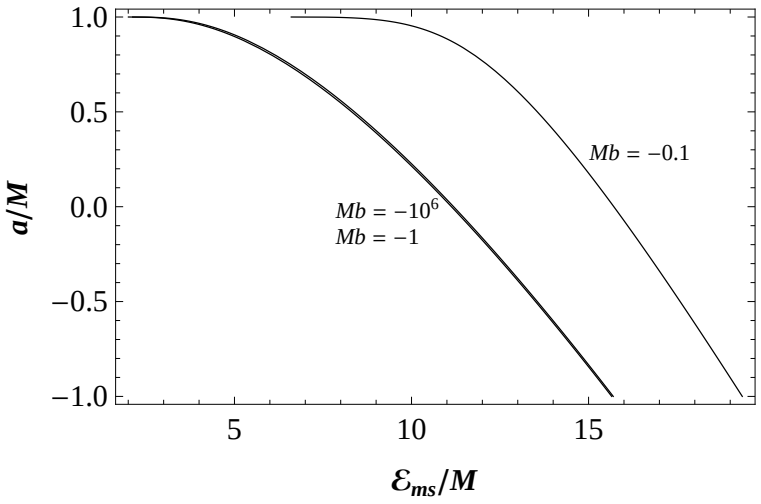

(**b**)

Figure 3.8: The ISCO's energy $\mathcal{E}_{ms}$ dependence on a for different values of the magnetic parameter b for (a) anti–Larmor and (b) Larmor motion.

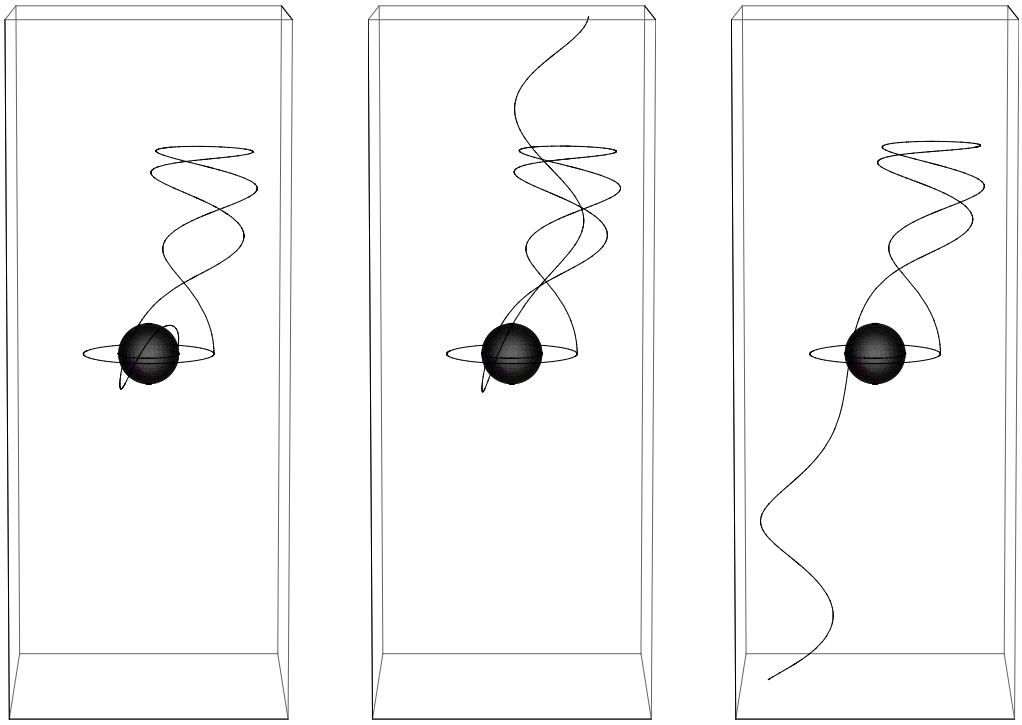

Figure 3.9: The trajectories of a charged particle initially at $r_o = 4M$ kicked to three different energies (a): $\mathcal{E} = 1.0890$ (b): $\mathcal{E} = 1.0893$ (c): $\mathcal{E} = 1.0900$. The black hole's spin parameter is $a = 0.5M$ and $b = 0.1M^{-1}$. The particle is scattered to a different final state in every case.

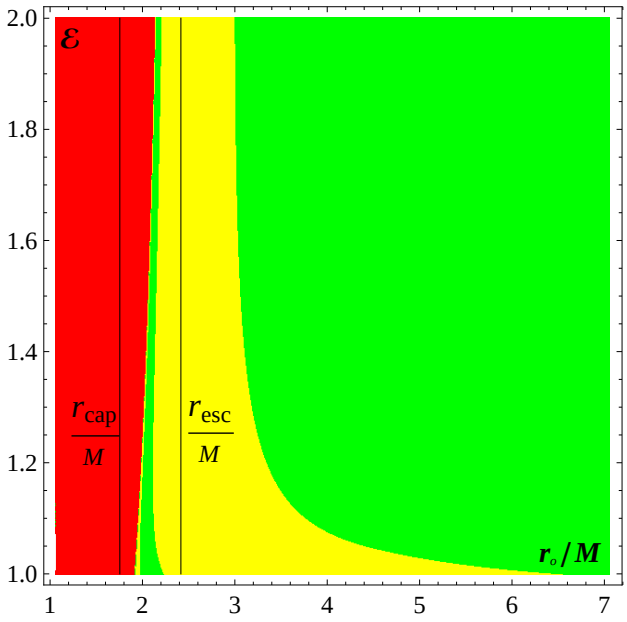

Figure 3.10: The basin of attraction for a neutral particle. r_{esc} and r_{cap} are shown as well. The black hole's rotation parameter is $a = 0.999M$.

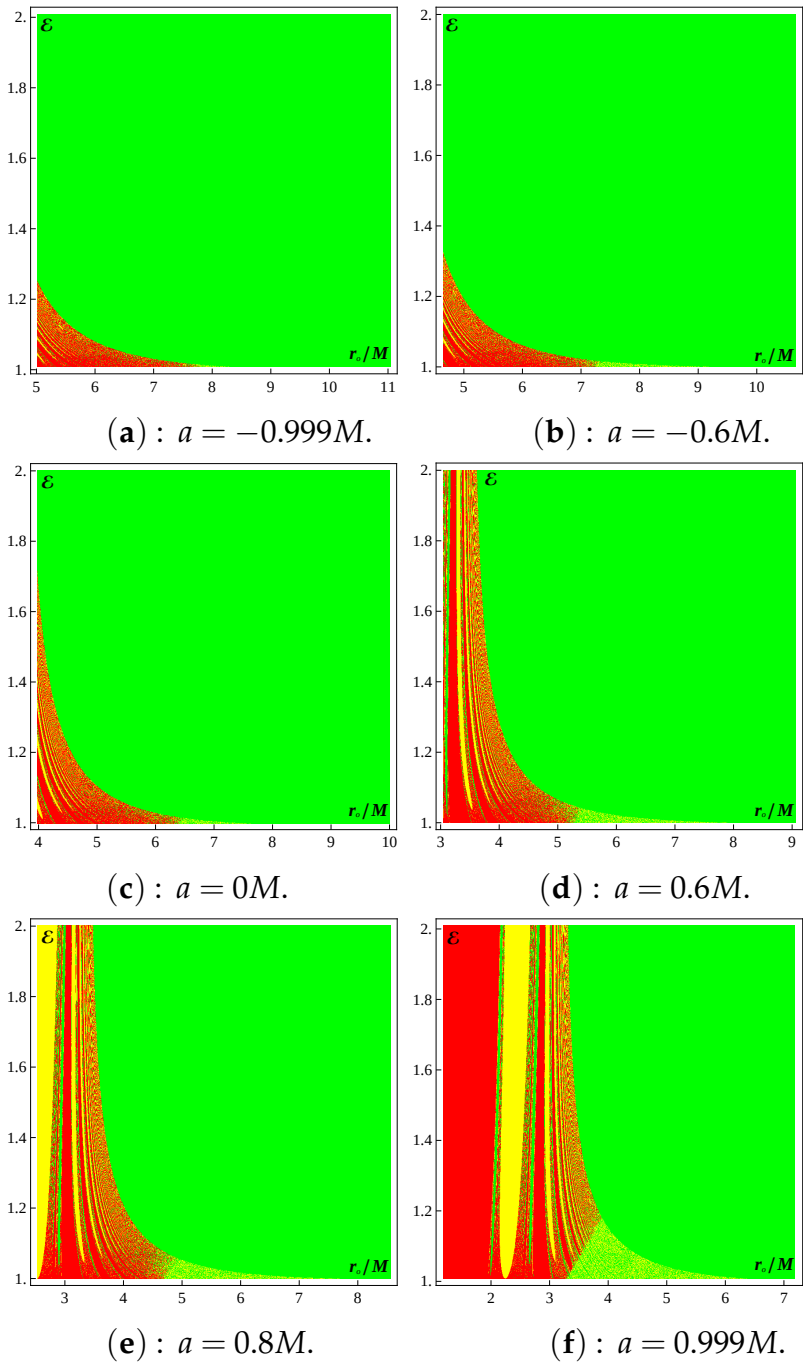

(**a**) : $a = -0.999M$. (**b**) : $a = -0.6M$.

(**c**) : $a = 0M$. (**d**) : $a = 0.6M$.

(**e**) : $a = 0.8M$. (**f**) : $a = 0.999M$.

Figure 3.11: The basins of attraction for a charged particle with $b = 0.1M^{-1}$ for selected a values.

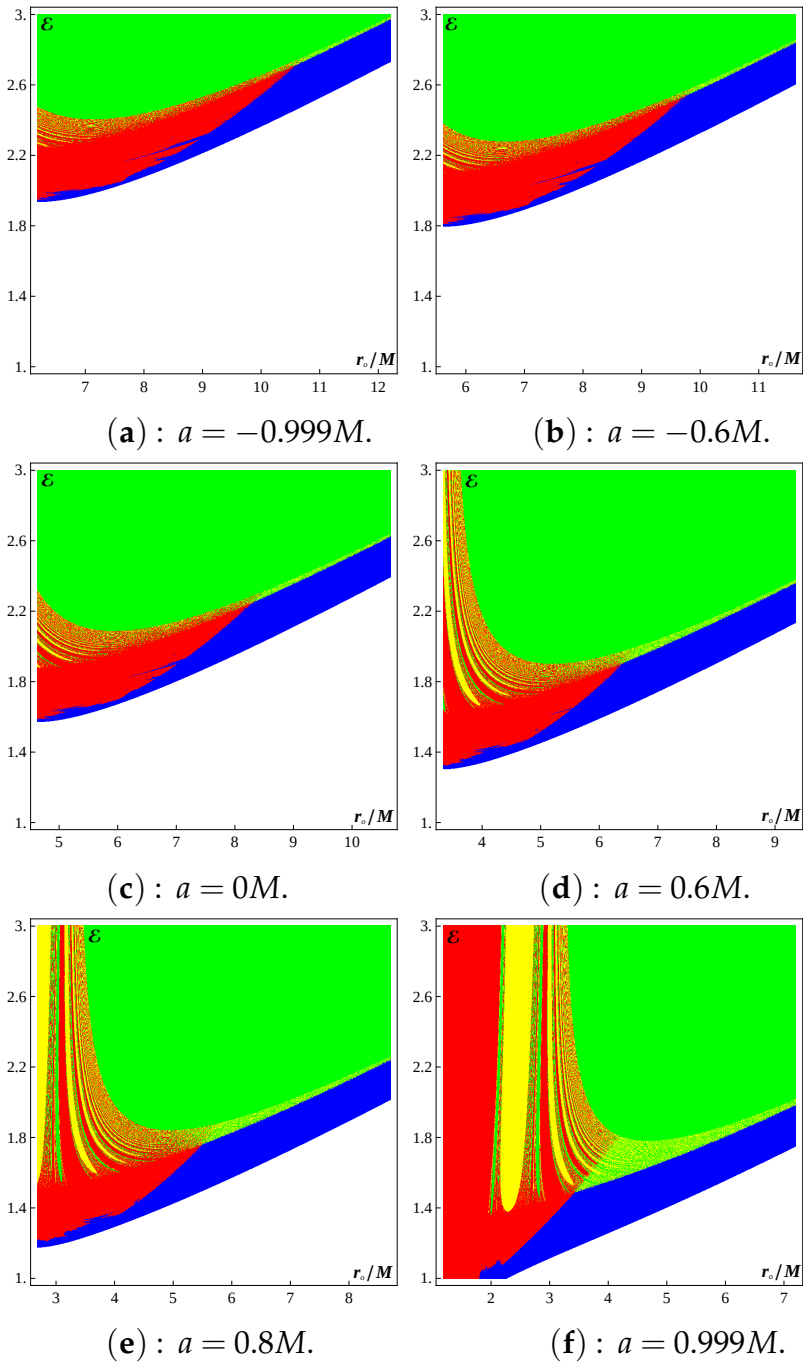

(**a**) : $a = -0.999M$. (**b**) : $a = -0.6M$.

(**c**) : $a = 0M$. (**d**) : $a = 0.6M$.

(**e**) : $a = 0.8M$. (**f**) : $a = 0.999M$.

Figure 3.12: The basins of attraction for a charged particle with $b = -0.1M^{-1}$ for selected a values.

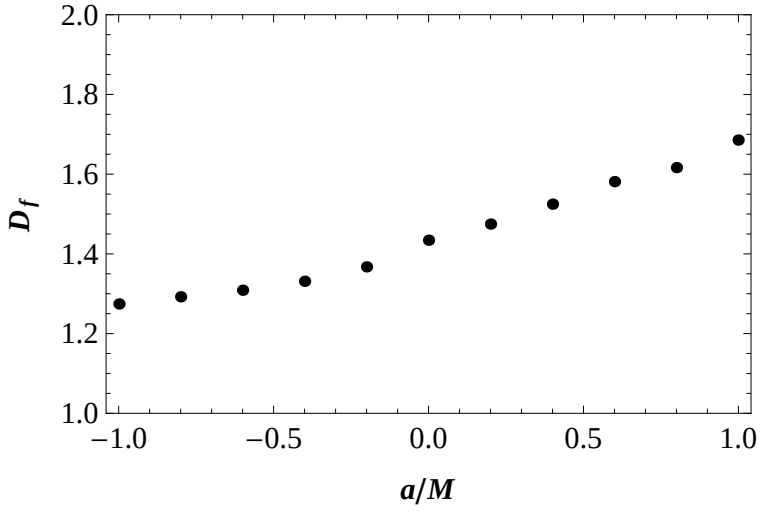

(**a**)

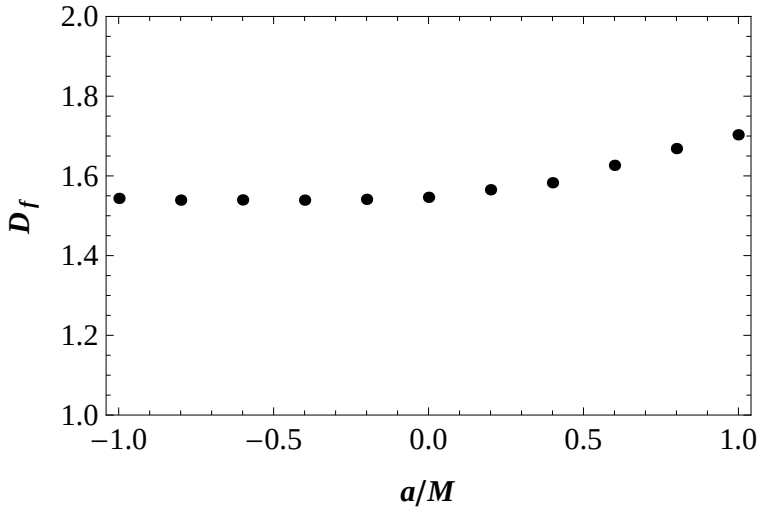

(**b**)

Figure 3.13: D_f of the basin boundaries vs. a for (a) anti-Larmor motion ($b = 0.1M^{-1}$) and (b) Larmor motion ($b = -0.1M^{-1}$).

Bibliography

[1] A. Zee, *Einstein Gravity in a Nutshell* (Princeton University Press, New Jersey, 2013).

[2] L. Brenneman, *Measuring the Angular Momentum of Supermassive Black Holes* (Springer Briefs in Astronomy, 2013).

[3] A. Prasanna and N. Dadhich, *Nuovo Cirnento* **72B**, 42 (1982).

[4] S. Dhurandhar and N. Dadhich, *Phys. Rev. D* **29**, 2712 (1984).

[5] S. Dhurandhar and N. Dadhich, *Phys. Rev. D* **30**, 1625 (1984).

[6] S. Parthasarathy, S. Wagh, S. Dhurandhar and N. Dadhich, *ApJ.* **307**, 38 (1986).

[7] A. N. Aliev and N. Özdemir, *Mon. Not. Roy. Astron. Soc.* **336**, 241 (2002).

Chapter 4

Conclusion

In this thesis we studied the escape of charged particles from a stable circular orbit around a weakly magnetized Schwarzschild and Kerr black holes. This problem can be relevant to the high energy emissions from astrophysical black holes, where magnetic fields play an essential role. We assumed that the field is uniform, axisymmetric and normal to the orbital plane. Essentially, we studied the three-dimensional motion of the particle after it is given a kick in the direction perpendicular to the plane of the orbit. The initial parameters of the particle are fixed by the orbit's radius. The set of initial conditions of the dynamics therefore consists of the initial radius and kick velocity (energy) $\{r_o, \mathcal{E}(\dot{\theta}_k)\}$. Mainly, the particle either gets captured by the black hole or escapes it and approach spatial infinity.

We started with neutral particles. When the black hole is not rotating, the particle always accelerates away after the kick and escapes if it is energetically free. When the black hole is rotating the particle's acceleration is always outward only if the particle's orbit is far enough from the black hole. If it is in the proximity of the black hole then it always accelerates inwardly. In between, the particle accelerates away if the velocity given to it by the kick is below some critical value. Since there is only one radial turning point, the particle can escape the black hole if it is made energetically free and accelerating outwardly. We referred to the outward and inward acceleration regions in the $\{r_o, \mathcal{E}(\dot{\theta}_k)\}$ space as the escape and

capture regions, respectively, and to the region in between as the critical escape region. The emergence of the escape and capture regions is due to the proximity of the initial orbit to the black hole while the emergence of the critical escape region is due to the black hole's rotation.

The problem when the particle is charged is more involved. The magnetic field breaks the general integrability of the equations of motion. The dynamics becomes generally chaotic. Additionally, the magnetic field brings the ISCO closer to the black hole. The effect of this is the possibility of the emergence of a capture region even when the black hole is not rotating. The chaoticness in the dynamics manifests itself in the boundaries between different regions of capture and escape. The boundaries become fractals instead of simple lines. This fact makes the analytical determination of the escape conditions formidable. We therefore used the boundary of the main escape region to set an effective escape condition.

There does not seem to be any lucid general relation between the black hole's rotation and the chaoticness in the dynamics. Instead, this kind of relations can be given in a restricted subset of the set of initial conditions of the dynamics. Nonetheless, the dynamics appears to be more chaotic near the black hole's horizon where the gravitational field is stronger.

It would be interesting to see how the problem changes when further sophistications are involved. Namely, when more realistic magnetic fields, more general initial orbits and more general kicks with physical kicking mechanisms are used. While these modifications may enrich the problem, we expect that its main features will be sustained.

Appendix A

Geometrized Units

We adopted in this thesis geometrical units in which the speed of light c and the gravitational constant G are set to unity. The dimensions of Length, Time and Mass are designated by L, T and M, respectively. A quantity with dimension $L^n T^m M^p$ in conventional units has the dimension L^{n+m+p} in geometrical units with the conversion factor $c^m (G/c^2)^p$ [1]. Table A.1 below lists some physical quantities of interest with the appropriate conversion factors.

Table A.1: Various physical quantities in conventional and geometrized units and the conversion factors.

Quantity	Conventional units	Geometrized units	Conversion factor
Length	L	L	1
Time	T	L	c
Velocity	LT^{-1}	1	c^{-1}
Acceleration	LT^{-2}	L^{-1}	c^{-2}
Mass	M	L	Gc^{-2}
Momentum	MLT^{-1}	L	Gc^{-3}
Angular Momentum	ML^2T^{-1}	L^2	Gc^{-3}

To express electromagnetic quantities in geometrized units we set the Coulomb constant $k_e = (4\pi\varepsilon_0)^{-1}$ equal to 1, where ε_0 is the electric permittivity of free space. We designate electric charge dimension by Q. A

quantity with dimension $L^n T^m M^p Q^q$ in conventional units has the dimension $L^{n+m+p+q}$ in geometrized units where the corresponding conversion factor is $c^{m-q}(G/c^2)^{p+q/2}k_e^{q/2}$. Table A.2 below lists a few interesting electromagnetic quantities with the appropriate conversion factors.

Table A.2: Some interesting electromagnetic quantities in conventional and geometrized units and the conversion factors.

Quantity	Conventional units	Geometrized units	Conversion factor
Electric charge	Q	L	$G^{1/2}k^{1/2}c^{-2}$
Electric current	TQ	L^2	$G^{1/2}k^{1/2}c^{-1}$
Electric field	$MLT^{-2}Q^{-1}$	L^{-1}	$G^{1/2}k^{-1/2}c^{-2}$
Magnetic field	$MT^{-1}Q^{-1}$	L^{-1}	$G^{1/2}k^{-1/2}c^{-1}$
Electric potential	$ML^2T^{-2}Q^{-1}$	1	$G^{1/2}k^{-1/2}c^{-2}$
Magnetic potential	$MLT^{-1}Q^{-1}$	1	$G^{1/2}k^{-1/2}c^{-1}$
qB/m[1]	T^{-1}	L^{-1}	c^{-1}

[1] R. Wald, *General Relativity* (The univerity of Chicago Press, Chicago, 1984).

[1] See Chapters 2 and 3 where this quantity is used.

Appendix B

Einstein-Maxwell Equations

In this Appendix we give a quick review of Einstein-Maxwell equations. The Einstein-Hilbert-Maxwell action reads

$$\mathcal{S}_{EHM} = \int (\mathcal{L}_{EH} + \mathcal{L}_{EM} + \mathcal{L}_I)\sqrt{-g}d^4x, \tag{1}$$

where

$$\mathcal{L}_{EH} = \frac{1}{16\pi}R, \tag{2}$$

$$\mathcal{L}_{EM} = -\frac{1}{16\pi}F^{\mu\nu}F_{\mu\nu}, \tag{3}$$

$$\mathcal{L}_I = j^\mu A_\mu. \tag{4}$$

Here R is the Ricci scalar, $F_{\mu\nu}$ is the electromagnetic field tensor given by $F_{\mu\nu} = A_{\nu,\mu} - A_{\mu,\nu}$ where A_μ is the electromagnetic four-potential and j^μ in the interaction term $\mathcal{L}_I$ is the electromagnetic four-current. Variation of the action with respect to $g^{\mu\nu}$ yields the Einstein field equations with the electromagnetic stress-energy tensor

$$R_{\mu\nu} - \frac{1}{2}g_{\mu\nu}R = 8\pi T^{(EM)}_{\mu\nu}, \tag{5}$$

where

$$T_{\mu\nu}^{(EM)} = \frac{1}{4\pi}\left(F_{\mu\alpha}F_{\nu}{}^{\alpha} - \frac{1}{4}g_{\mu\nu}F_{\beta\gamma}F^{\beta\gamma}\right). \tag{6}$$

To get the Maxwell equations in the curved background described by $g_{\mu\nu}$ we variate the action with respect to the vector potential A^{μ}. The variation yields

$$F^{\mu\nu}{}_{;\mu} = 4\pi j^{\nu}. \tag{7}$$